JOURNAL OF GEOPHYSICAL RESEARCH: ATMOSPHERES, VOL. 118, 8086–8110, doi:10.1002/jgrd.50608, 2013

Impact of preindustrial to present-day changes in short-lived pollutant emissions on atmospheric composition and climate forcing

Vaishali Naik,[1] Larry W. Horowitz,[2] Arlene M. Fiore,[3] Paul Ginoux,[2] Jingqiu Mao,[4] Adetutu M. Aghedo,[5] and Hiram Levy II[2]

Received 23 January 2013; revised 24 June 2013; accepted 24 June 2013; published 30 July 3013.

[1] We describe and evaluate atmospheric chemistry in the newly developed Geophysical Fluid Dynamics Laboratory chemistry-climate model (GFDL AM3) and apply it to investigate the net impact of preindustrial (PI) to present (PD) changes in short-lived pollutant emissions (ozone precursors, sulfur dioxide, and carbonaceous aerosols) and methane concentration on atmospheric composition and climate forcing. The inclusion of online troposphere-stratosphere interactions, gas-aerosol chemistry, and aerosol-cloud interactions (including direct and indirect aerosol radiative effects) in AM3 enables a more complete representation of interactions among short-lived species, and thus their net climate impact, than was considered in previous climate assessments. The base AM3 simulation, driven with observed sea surface temperature (SST) and sea ice cover (SIC) over the period 1981–2007, generally reproduces the observed mean magnitude, spatial distribution, and seasonal cycle of tropospheric ozone and carbon monoxide. The global mean aerosol optical depth in our base simulation is within 5% of satellite measurements over the 1982–2006 time period. We conduct a pair of simulations in which only the short-lived pollutant emissions and methane concentrations are changed from PI (1860) to PD (2000) levels (i.e., SST, SIC, greenhouse gases, and ozone-depleting substances are held at PD levels). From the PI to PD, we find that changes in short-lived pollutant emissions and methane have caused the tropospheric ozone burden to increase by 39% and the global burdens of sulfate, black carbon, and organic carbon to increase by factors of 3, 2.4, and 1.4, respectively. Tropospheric hydroxyl concentration decreases by 7%, showing that increases in OH sinks (methane, carbon monoxide, nonmethane volatile organic compounds, and sulfur dioxide) dominate over sources (ozone and nitrogen oxides) in the model. Combined changes in tropospheric ozone and aerosols cause a net negative top-of-the-atmosphere radiative forcing perturbation ($-1.05\ \mathrm{W\,m^{-2}}$) indicating that the negative forcing (direct plus indirect) from aerosol changes dominates over the positive forcing due to ozone increases, thus masking nearly half of the PI to PD positive forcing from long-lived greenhouse gases globally, consistent with other current generation chemistry-climate models.

Citation: Naik, V., L. W. Horowitz, A. M. Fiore, P. Ginoux, J. Mao, A. M. Aghedo, and H. Levy II (2013), Impact of preindustrial to present-day changes in short-lived pollutant emissions on atmospheric composition and climate forcing, *J. Geophys. Res. Atmos.*, *118*, 8086–8110, doi:10.1002/jgrd.50608.

1. Introduction

[2] Although long-lived greenhouse gases in the atmosphere are the dominant contributors to climate change, short-lived climate forcing agents including tropospheric ozone (O_3) and sulfate and carbonaceous aerosols have also contributed considerably to the radiative forcing of climate since preindustrial times [*Forster et al.*, 2007]. Several studies have demonstrated the importance of future evolution of short-lived climate forcers on the climate system [*Shindell et al.*, 2007, 2008; *Levy et al.*, 2008, 2013; *Menon et al.*, 2008; *Liao et al.*, 2009], yet the net climate impact of these species from preindustrial (PI) to present day (PD) is quite uncertain not only because of the uncertainties in their emission estimates and atmospheric burdens, but also due to their competing radiative effects. For example, increases

Additional supporting information may be found in the online version of this article.

[1]UCAR/NOAA Geophysical Fluid Dynamics Laboratory, Princeton, New Jersey, USA.
[2]NOAA Geophysical Fluid Dynamics Laboratory, Princeton, New Jersey, USA.
[3]Department of Earth and Environmental Sciences and Lamont-Doherty Earth Observatory, Columbia University, Palisades, New York, USA.
[4]Atmospheric and Oceanic Sciences, Princeton University, Princeton, New Jersey, USA.
[5]Civil and Environmental Engineering, Rice University, Houston, Texas, USA.

Corresponding author: V. Naik, UCAR/NOAA Geophysical Fluid Dynamics Laboratory, 201 Forrestal Rd., Princeton, NJ 08540, USA. (Vaishali.Naik@noaa.gov)

2169-897X/13/10.1002/jgrd.50608

in tropospheric ozone and black carbon contribute to climate warming, while increases in sulfate and organic carbon cool the Earth's climate [*Forster et al*., 2007; *Koch et al*., 2009, 2011]. Additionally, aerosols affect the radiation budget indirectly by interacting with clouds, resulting in either a warming or cooling [*Lohmann and Feichter*, 2005; *Forster et al*., 2007; *Koch and Del Genio*, 2010; *Mahowald et al*., 2011]. The goal of this study is to document and evaluate tropospheric chemistry in the newly developed Geophysical Fluid Dynamics Laboratory chemistry-climate model (GFDL AM3) and apply it to investigate the net impact of PI to PD changes in short-lived pollutant emissions on atmospheric composition and climate forcing. The inclusion of online troposphere-stratosphere interactions, gas-aerosol chemistry, and aerosol-cloud interactions (including direct and indirect aerosol radiative effects) in AM3 enables a more complete representation of interactions among short-lived species, and thus their net climate impact, than was considered in previous climate assessments [e.g., *Forster et al*., 2007].

[3] Short-lived pollutants interact in many ways to influence the atmospheric chemical composition and the Earth's radiation budget [*Isaksen et al*., 2009]. Changes in emissions of tropospheric ozone precursors, including nitrogen oxides (NO_x), carbon monoxide (CO), methane (CH_4), and nonmethane volatile organic compounds (NMVOCs), influence the abundance of tropospheric ozone and its radiative forcing on climate. In addition, they affect the oxidizing capacity of the atmosphere, thereby influencing the lifetime of CH_4, itself a near-term climate forcer and an ozone precursor [*Fuglestvedt et al*., 1999; *Wild et al*., 2001; *Fiore et al*., 2002; *Naik et al*., 2005; *West et al*., 2007]. Changes in the oxidant levels (driven by changes in ozone and its precursors) can also impact the atmospheric burden of aerosols [*Liao et al*., 2003; *Unger et al*., 2006; *Bauer et al*., 2007]. Changes in aerosol burdens, either induced by chemistry or via direct controls on their (or their precursor) emissions, impact heterogeneous chemistry, modify the atmospheric radiation budget, and alter cloud properties, influencing ozone photochemistry [*Martin et al*., 2003; *Bian et al*., 2003; *Lamarque et al*., 2005a; *Menon et al*., 2008; *Unger et al*., 2009] and the hydrological cycle [*Lohmann and Feichter*, 2005; *Rosenfeld et al*., 2008]. Furthermore, anthropogenic emissions of short-lived pollutants are strongly tied to economic development and modulated by air pollution controls. Spatially heterogeneous emissions combined with nonlinear chemical interactions result in strong spatial and temporal gradients of short-lived climate forcers and, in turn, an inhomogeneous, highly uncertain climate response.

[4] Prior studies investigating the climate impact of short-lived pollutants generally relied on chemistry-transport models (CTMs) to first simulate the atmospheric distributions of short-lived species and then imposed these precomputed distributions in a radiation or climate model to calculate the resulting climate forcing or response [*Forster et al*., 2007]. The recent development of coupled chemistry-climate models has enabled simulations of aerosol-ozone-climate interactions and feedbacks, thus providing an improved understanding of the role of short-lived climate forcers in the climate system. For example, *Liao et al*. [2009] applied a coupled global atmosphere-tropospheric chemistry-aerosol model with a simplified ocean module to investigate the impact of future ozone and aerosols on tropospheric composition and climate, while *Koch et al*. [2011] studied the impact of historical changes in ozone and aerosols using a fully coupled global ocean-atmosphere-aerosol-chemistry model. Although the models of *Liao et al*. [2009] and *Koch et al*. [2011] are much advanced than those applied in previous studies [*Forster et al*., 2007; *Levy et al*., 2008], neither considered aerosol indirect radiative effects which could alter their estimates.

[5] Here, we build upon earlier studies by applying the GFDL AM3, a newly developed chemistry-climate model that includes troposphere-stratosphere coupling, gas-aerosol chemistry, and aerosol-cloud interactions, to investigate the effects of short-lived pollutant emissions on climate forcing. Specifically, we assess the changes in atmospheric composition and the impact on climate forcing resulting from the PI (1860) to PD (2000) changes in short-lived pollutants (emissions of ozone precursors, SO_2 and carbonaceous aerosols, and CH_4 concentration) with fixed sea surface temperatures (SSTs). This experimental setup allows us to simulate the fast atmospheric responses from combined changes in ozone and aerosols, which we diagnose as radiative forcing perturbation (RFP) following *Hansen et al*. [2005]. RFP has been shown to be a better indicator of the climate response to short-lived forcings than the traditional radiative forcing [*Hansen et al*., 2005; *Lohmann et al*., 2010]. In section 2, we describe the key features of the AM3 model and discuss the emissions and boundary conditions implemented in the model. We evaluate the results of a base simulation against observations in section 3. The impact of PI to PD changes in short-lived pollutant emissions and CH_4 concentration on atmospheric composition and climate forcing is presented in section 4. Finally, overall results are discussed and conclusions are drawn in section 5.

2. Model Description

[6] The AM3 model, the atmospheric component of the GFDL coupled model (CM3) [*Donner et al*., 2011; *Griffies et al*., 2011], is developed from the GFDL AM2 model [*GFDL Global Atmospheric Model Development Team*, 2004, hereafter GAMDT04] and has been applied recently to address key questions in chemistry-climate interactions [*Fang et al*., 2011; *Rasmussen et al*., 2012; *John et al*., 2012; *Turner et al*., 2013]. In addition to the dynamical and physical updates described by *Donner et al*. [2011], the primary new feature of the model is that it simulates tropospheric and stratospheric chemistry interactively (with feedback to atmospheric radiation) over the full model domain. This unified representation of tropospheric and stratospheric chemistry in AM3 obviates prescribing the concentrations of chemical species important for calculating radiation balance as previously done (GAMDT04 [*Delworth et al*., 2006]), thereby removing inconsistencies between the model-generated meteorology and the atmospheric distributions of the forcing agents. The model uses a finite-volume dynamical core on a horizontal domain consisting of, in its standard configuration, $6 \times 48 \times 48$ cubed-sphere grid with the grid size varying from 163 km (at the six corners of the cubed sphere) to 231 km (near the center of each face), a resolution denoted as C48. The vertical domain of the model extends from the surface up to 0.01 hPa (86 km) with 48 vertical hybrid sigma pressure levels. Chemical species undergo transport (advection, vertical diffusion, and

convection) in accordance with the AM3 model physics as described by *Donner et al*. [2011]. An additional key feature of the AM3 model physics is that it represents aerosols and clouds in a self-consistent way [*Ming and Ramaswamy*, 2009; *Donner et al*., 2011; *Golaz et al*., 2011], thus accounting for aerosol-cloud interactions and indirect effects of aerosols. Below we describe in detail the chemistry represented in AM3.

2.1. Chemistry

[7] Tropospheric trace gas chemistry in AM3 is based on a modified version of the chemical scheme used in the Model for OZone and Related Tracers version 2 (MOZART-2) [*Horowitz et al*., 2003, 2007]. It includes reactions of NO_x-HO_x-O_x-CO-CH_4 and other NMVOCs. Sulfate aerosols are produced chemically in the model via the fully coupled gas and aqueous phase oxidation of SO_2 by OH, O_3, and H_2O_2 and the gas-phase oxidation of dimethyl sulfide (DMS). Organic carbonaceous aerosols are modeled as directly emitted primary organic aerosols (POA) and secondary organic aerosols (SOA) formed by the oxidation of natural and anthropogenic NMVOCs. The natural source of SOA includes 30.4 Tg C yr^{-1} produced from the rapid oxidation of biogenic terpenes based on *Dentener et al*. [2006], and the anthropogenic source includes 9.6 Tg C yr^{-1} from the OH-induced oxidation of butane calculated following *Tie et al*. [2005]. Both the natural and anthropogenic SOA sources have been calculated offline and do not vary with time in the current version of the model. Black carbon and primary organic carbon are converted from hydrophobic to hydrophilic state with an e-folding time of 1.44 days, within the range of values previously applied in global models [*Kanakidou et al*., 2005]. Nitrate aerosols are simulated but do not impact radiation calculations in this version of the model. Recent studies estimate that PI to PD changes in nitrate aerosols have contributed only slightly to the aerosol forcing on climate although future reductions in sulfate precursors combined with increases in the emissions of ammonia may lead to a stronger role of nitrate aerosols in the coming decades [*Bauer et al*., 2007; *Bellouin et al*., 2011]. The size distribution of sea salt and mineral dust aerosols is represented by five size bins each, ranging from 0.1 to 10 μm (dry radius).

[8] Representation of stratospheric chemistry is based on the formulation of *Austin and Wilson* [2010] that includes the major stratospheric ozone loss cycles (O_x, HO_x, NO_x, ClO_x, and BrO_x) and heterogeneous reactions on sulfate aerosols (liquid ternary solutions) and polar stratospheric clouds (nitric acid trihydrate (NAT) and water-ice). Heterogeneous reactions on liquid ternary solutions are represented based on *Carslaw et al*. [1995], and those on NAT polar stratospheric clouds are calculated as in *Hanson and Mauersberger* [1988]. The rates of change of inorganic chlorine (Cl_y) and inorganic bromine (Br_y) are parameterized as a function of tropospheric concentrations of source gases (CFC11, CFC12, CH_3Cl, CCl_4, CH_3CCl_3, and HCFC22 for Cl_y, and CH_3Br, Halon1211, and Halon1301 for Br_y) for computational efficiency to avoid transporting additional tracers in the model (discussed in detail by *Austin et al*., 2013). Changes in stratospheric ozone and water vapor feedback to the atmospheric radiation, thereby coupling the climate and chemistry.

[9] The model simulates the atmospheric concentrations of 97 chemical species listed in Table 1 throughout the model domain, of which 16 are aerosol species, undergoing 171 gas-phase reactions, 41 photolytic reactions, and 16 heterogeneous reactions in the model. Kinetic reaction rates are based on JPL 2006 [*Sander et al*., 2006]. Clear-sky photolysis frequencies are computed using a multivariate interpolation table resulting from calculations using the Tropospheric Ultraviolet and Visible radiation model version 4.4 [*Madronich and Flocke*, 1998]. Photolysis frequencies are adjusted for simulated overhead stratospheric ozone column, surface albedo, and clouds but do not account for simulated aerosols. The chemical system is solved numerically using a fully implicit Euler backward method with Newton-Raphson iteration, as in *Horowitz et al*. [2003]. Changes in tropospheric ozone and aerosols feedback to atmospheric radiation.

2.2. Deposition

[10] Except for ozone and peroxyacetyl nitrate (PAN), monthly mean dry deposition velocities of gaseous species (shown with a superscript letter "a" in Table 1) are from *Horowitz et al*. [2003] calculated offline using a resistance-in-series scheme [*Wesely*, 1989; *Hess et al*., 2000]. Dry deposition velocities for ozone are taken from *Bey et al*. [2001], and those for PAN are from a simulation of MOZART version 4 that included updates to the resistance-in-series scheme as described by *Emmons et al*. [2010]. A diurnal cycle is imposed on the monthly mean deposition velocity for ozone as in *Horowitz et al*. [2003]. Dry deposition of aerosols includes gravitational settling and impaction at the surface by turbulence [*Li et al*., 2008; *Donner et al*., 2011].

[11] Wet deposition of soluble gaseous species includes in-cloud and below-cloud scavenging by large-scale (ls) and convective clouds (cv) and is simulated as first-order loss processes. In-cloud scavenging of soluble gases (shown with a superscript letter "b" in Table 1) is calculated using the scheme of *Giorgi and Chameides* [1985]. Below-cloud wet scavenging is only considered for large-scale precipitation and is computed for gases following Henry's law as described in *Brasseur et al*. [1998]. The wet deposition parameterization of gases and aerosols in AM3 is summarized by *Donner et al*. [2011], with additional details provided here in Appendix A.

2.3. Emissions and Lower Boundary Conditions

[12] Surface emissions of chemical species are from the new emissions data set of *Lamarque et al*. [2010], developed for chemistry-climate model simulations for the Climate Model Intercomparison Project Phase 5 (CMIP5) in support of the Intergovernmental Panel on Climate Change (IPCC) Fifth Assessment Report (AR5). The inventory provides monthly mean gridded emissions of reactive chemical species, including ozone precursors and aerosols (and their precursors), at a horizontal resolution of 0.5° latitude × 0.5° longitude for each decade beginning from 1850 to 2000. Emissions originating from anthropogenic sources (defined to include energy use in stationary and mobile sources, industrial processes, and domestic and agricultural activities), open biomass burning (includes burning of grasslands and forests), ships, and aircraft are provided. Surface anthropogenic emissions for the base year 2000 are generated by aggregating existing regional and global emission inventories

Table 1. Chemical Species Included in AM3

No.	Species Name	Chemical Formula	Details
		Transported	
1	O_3[a]	O_3	ozone
2	N2O	N_2O	nitrous oxide
3	NO	NO	nitric oxide
4	NO2[a]	NO_2	nitrogen dioxide
5	NO3	NO_3	nitrate radical
6	HNO3[a,b]	HNO_3	nitric acid
7	HO2NO2[a,b]	HNO_4	pernitric acid
8	N2O5	N_2O_5	dinitrogen pentaoxide
9	CH_4[a]	CH_4	methane
10	CH3OOH[a]	CH_3OOH	methyl hydroperoxide
11	CH2O[a,b]	HCHO	formaldehyde
12	CO[a]	CO	carbon monoxide
13	H2O2[a,b]	H_2O_2	hydrogen peroxide
14	C3H6	C_3H_6	propene
15	ISOP	C_5H_8	isoprene
16	CH3CHO[a,b]	CH_3CHO	acetaldehyde
17	POOH[b]	C_3H_6OHOOH	
18	CH3COOOH[a,b]	CH_3COOOH	peracetic acid
19	PAN[a]	$CH_3CO_3NO_2$	peroxy acetyl nitrate
20	ONIT[b]	$CH_3COCHO_2CH_2OHNO$	
21	C2H6	C_2H_6	ethane
22	C2H4	C_2H_4	ethene
23	C4H10	C_4H_{10}	lumped alkanes as $C \geq 4$
24	MPAN	$CH_2CCH_3CO_3NO_2$	methacryloyl peroxynitrate
25	MVK[b]	$CH_2CHCOCH_3$	methyl vinyl ketone
26	MACR[b]	CH_2CCH_3CHO	methacrolein
27	MACROOH[b]	$CH_3COCH(OOH)CH_2OH$	
28	C2H5OOH[b]	C_2H_5OOH	ethyl hydroperoxide
29	C10H16	$C_{10}H_{16}$	lumped monoterpenes as α-pinene
30	C3H8	C_3H_8	propane
31	C3H7OOH[b]	C_3H_7OOH	propyl hydroperoxide
32	CH3COCH3[a]	CH_3COCH_3	acetone
33	ROOH[b]	CH_3COCH_2OOH	
34	CH3OH[b]	CH_3OH	methanol
35	C2H5OH[b]	C_2H_5OH	ethanol
36	GLYALD[b]	$HOCH_2CHO$	glycolaldehyde
37	HYAC[b]	CH_3COCH_2OH	hydroxyacetone
38	HYDRALD[b]	$HOCH_2CCH_3CHCHO$	lumped unsaturated hydroxycarbonyl
39	CH3COCHO[a,b]	CH_3COCHO	methyl glyoxal
40	ONITR[b]	$CH_2CCH_3CHONO_2CH_2OH$	lumped isoprene nitrate
41	XOOH[b]	$HOCH_2C(OOH)CH_3CH(OH)CHO$	
42	ISOPOOH[b]	$HOCH_2C(OOH)CH_3CHCH_2$	unsaturated hydroxyhydroperoxide
43	H2	H_2	molecular hydrogen
44	SO2[b]	SO_2	sulfur dioxide
45	SO4	SO_4^{2-}	sulfate
46	DMS[b]	CH_3SCH_3	dimethyl sulfide
47	NH3[b]	NH_3	ammonia
48	NH4NO3	NH_4NO_3	ammonium nitrate
49	NH4	NH_4^+	ammonium
50	SOA		secondary organic aerosol
51	dust1	dust	dust dry radius 0.1–1.0 μm
52	dust2	dust	dust dry radius 1.0–1.8 μm
53	dust3	dust	dust dry radius 1.8–3.0 μm
54	dust4	dust	dust dry radius 3.0–6.0 μm
55	dust5	dust	dust dry radius 6.0–10.0 μm
56	ssalt1	sea salt	sea salt dry radius 0.1–1.0 μm
57	ssalt2	sea salt	sea salt dry radius 1.0–1.8 μm
58	ssalt3	sea salt	sea salt dry radius 1.8–3.0 μm
59	ssalt4	sea salt	sea salt dry radius 3.0–6.0 μm
60	ssalt5	sea salt	sea salt dry radius 6.0–10.0 μm
61	bcphob	black carbon	hydrophobic fraction of black carbon
62	bcphil	black carbon	hydrophilic fraction of black carbon
63	omphob	organic matter	hydrophobic fraction of organic matter
64	omphil	organic matter	hydrophilic fraction of organic matter
65	HCl[b]	HCl	hydrochloric acid
66	HOCl	HOCl	hypochlorous acid
67	ClONO2	$ClONO_2$	chlorine nitrate
68	Cl	Cl	elemental chlorine
69	ClO	ClO	chlorine monoxide
70	Cl2O2	Cl_2O_2	chlorine monoxide dimer
71	Cl2	Cl_2	molecular chlorine

Table 1. (continued)

No.	Species Name	Chemical Formula	Details
72	HOBr	HOBr	hypobromous acid
73	HBr[b]	HBr	hydrobromic acid
74	BrONO2	$BrONO_2$	bromine nitrate
75	Br	Br	elemental bromine
76	BrO	BrO	bromine monoxide
77	BrCl	BrCl	bromine monochloride
78	H2O	H_2O	water
		Not Transported	
79	O	$O(^3P)$	ground state atomic oxygen
80	O1D	$O(^1D)$	excited state atomic oxygen
81	OH	OH	hydroxyl radical
82	HO2	HO_2	hydroperoxyl radical
83	CH3O2	CH_3O_2	methyl peroxy radical
84	ISOPO2	$HOCH_2C(OO)CH_3CHCH_2$	peroxy radical derived from OH + ISOP
85	CH3CO3	CH_3CO_3	acetylperoxy radical
86	MACRO2	$CH_3COCH(OO)CH_2OH$	peroxy radical from OH addition to MVK, MACR
87	EO2	$HOCH_2CH_2O_2$	
88	EO	$HOCH_2CH_2O$	
89	MCO3	$CH_2CCH_3CO_3$	peroxy radical from reaction of OH with MACR
90	RO2	CH_3COCH_2O2	1-methyl vinoxy radical
91	C2H5O2	$C_2H_5O_2$	ethyl peroxy radical
92	ISOPNO3	$CH_2CHCCH_3OOCH_2ONO_2$	peroxy isoprene nitrate
93	XO2	$HOCH_2C(OO)CH_3CH(OH)CHO$	peroxy radical from OH + HYDRALD
94	PO2	$C_3H_6OHO_2$	
95	C3H7O2	$C_3H_7O_2$	propyl peroxy radical
96	H	H	hydrogen
97	N	N	elemental nitrogen

[a]Gaseous species that undergo dry deposition in AM3.
[b]Soluble gaseous species that undergo wet deposition in AM3.

for 40 world regions and 10 sectors (see *Lamarque et al.* [2010] for more details). Monthly emissions are given for all sources; however, there is no seasonal variation in anthropogenic and ship emissions. Since no information on the vertical distribution of biomass burning emissions was provided in the original data set, we followed the recommendations of *Dentener et al.* [2006] to distribute these emissions over six ecosystem-dependent altitude levels between the surface and 6 km. Emissions from agricultural waste burning and fuelwood burning, which are usually specified with biomass burning, are included in anthropogenic residential sector emissions.

Table 2. Emissions of Short-Lived Species in AM3 for Year 2000[a]

Species	Anthropogenic	Biomass Burning	Biogenic Soil	Oceans	Ship	Total
NO_x (Tg N yr^{-1})	26.5 (0.7)	5.5 (4.8)	3.6 (3.6)	0.0 (0.0)	5.4 (0.1)	41.0 (9.3)
CO (Tg yr^{-1})	608.3 (67.3)	459.1 (322.6)	159.3 (159.3)	19.8 (19.8)	1.2 (0.03)	1247.7 (569.0)
C_2H_4 (Tg C yr^{-1})	6.4 (1.1)	5.4 (3.6)	4.3 (4.3)	1.2 (1.2)	0.2 (0.01)	17.5 (10.2)
C_2H_6 (Tg C yr^{-1})	2.6 (0.5)	2.5 (1.5)	0.8 (0.8)	0.8 (0.8)	0.12 (0.0)	6.8 (3.5)
C_3H_6 (Tg C yr^{-1})	7.7 (1.0)	4.7 (2.8)	0.9 (0.9)	1.3 (1.3)	0.3 (0.01)	14.9 (6.0)
C_3H_8 (Tg C yr^{-1})	2.8 (0.2)	1.6 (0.5)	1.6 (1.6)	1.0 (1.0)	0.4 (0.01)	7.4 (3.4)
CH_2O (Tg C yr^{-1})	3.2 (0.1)	5.8 (4.0)	0.0 (0.0)	0.0 (0.0)	0.0 (0.0)	9.0 (4.1)
Acetone (Tg C yr^{-1})	2.2 (0.0)	2.9 (2.4)	24.3 (24.3)	0.0 (0.0)	0.0 (0.0)	29.4 (26.8)
CH_3OH (Tg C yr^{-1})	0.8 (0.1)	11.9 (7.6)	228.2 (228.2)	0.0 (0.0)	0.0 (0.0)	240.9 (236.0)
C_2H_5OH (Tg C yr^{-1})	4.5 (0.6)	0.1 (0.05)	9.2 (9.2)	0.0 (0.0)	0.0 (0.0)	13.8 (9.9)
C_4H_{10} (Tg C yr^{-1})	43.0 (0.6)	0.9 (0.7)	0.0 (0.0)	0.0 (0.0)	1.2 (0.03)	45.1 (1.3)
Isoprene (Tg C yr^{-1})	0.0 (0.0)	0.8 (0.3)	564.7 (564.7)	0.0 (0.0)	0.0 (0.0)	565.5 (565.1)
Terpenes (Tg C yr^{-1})	0.0 (0.0)	0.4 (0.2)	143.2 (143.2)	0.0 (0.0)	0.0 (0.0)	143.6 (143.4)
H_2 (Tg yr^{-1})	21.3 (2.2)	9.6 (5.2)	3.0 (3.0)	3.0 (3.0)	0.0 (0.0)	36.9 (13.4)
NH_3[b] (Tg yr^{-1})	37.5 (7.3)	10.5 (6.1)	3.1 (3.1)	9.9 (9.9)	0.0 (0.0)	61.0 (26.5)
SO_2 (Tg S yr^{-1})	46.4 (1.5)	1.9 (1.2)	0.0 (0.0)	0.0 (0.0)	5.5 (0.1)	53.8 (2.8)
BC (Tg C yr^{-1})	5.0 (1.3)	2.6 (2.0)	0.0 (0.0)	0.0 (0.0)	0.1 (0.0)	7.7 (3.3)
OM (Tg C yr^{-1})	29.7[c] (18.0)[c]	37.2 (28.8)	30.4 (30.4)	15.5(15.4)	0.2 (0.0)	113.0 (92.6)
Aircraft NO (Tg N yr^{-1})						0.8 (0.0)
Aircraft SO_2 (Tg yr^{-1})						0.1 (0.0)
Fuel use (Tg yr^{-1})						122.0 (0.0)
Dust (Tg yr^{-1})						1221 (1237)
Sea salt (Tg yr^{-1})						6188 (6324)
Dimethyl sulfide (Tg yr^{-1})						36.2 (36.0)

[a]Emissions for year 1860 are shown in parentheses.
[b]Emissions of NH_3 also include 0.1 Tg yr^{-1} from animals.
[c]Includes a constant source of 9.6 Tg C yr^{-1} as SOA produced from the oxidation of butane calculated offline.

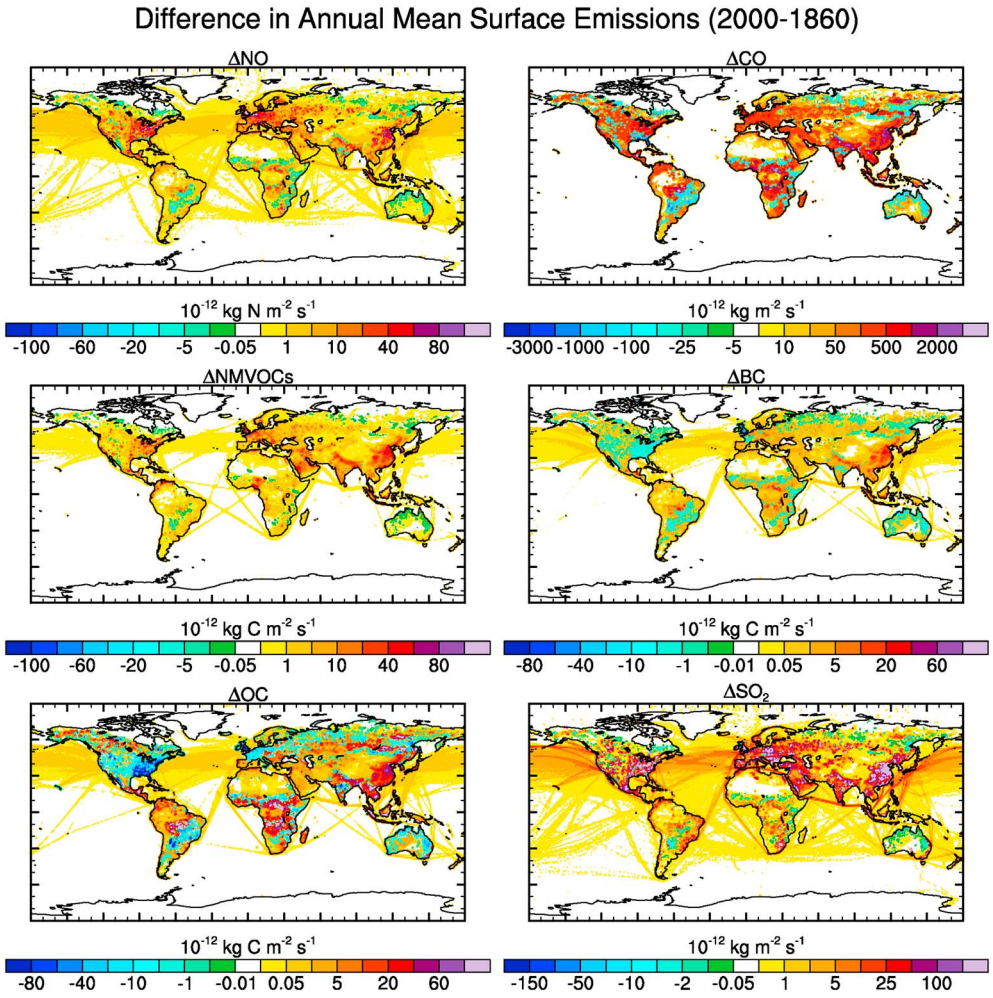

Figure 1. Change in annual mean surface emissions from 1860 to 2000 for nitrogen oxide (NO), carbon monoxide (CO), nonmethane volatile organic compounds (NMVOCs), black carbon (BC), organic carbon (OC), and sulfur dioxide (SO_2). Surface emissions include emissions from anthropogenic sources, biomass burning, and ships.

[13] The inventory includes ship emissions from international and domestic shipping and fishing, which are based on a recent assessment by *Eyring et al*. [2009]. As noted by *Lamarque et al*. [2010], the spatial distribution of ship emissions does not account for dispersion, chemical transformation, and subgrid-scale loss processes, which may lead to an overestimate of ozone formation in global models. The inventory also includes aircraft emissions of nitrogen oxide and black carbon based on calculations using the FAST model [*Lee et al*., 2005] for the European Quantify project (http://www.pa.op.dlr.de/quantify/). Emissions are provided at altitude levels from about 0.3 to 15 km. As aircraft SO_2 emissions are not provided in the inventory, we calculate these by scaling the aircraft emissions of black carbon (BC) by an emission ratio of 25 g SO_2/g BC [*Henderson et al*., 1999; *Hendricks et al*., 2004].

[14] Estimates of emissions from natural sources, including plants, soils, or oceans, are not provided by *Lamarque et al*. [2010]. We, therefore, use natural emissions (biogenic/soil and oceanic sources in Table 2) for gaseous species, including isoprene, from the Precursors of Ozone and their Effects in the Troposphere inventory for PD (corresponding to year 2000) [*Granier et al*., 2005; *Emmons et al*., 2010]. Natural emissions vary from month to month; however, they do not respond to changes in climate, vegetation, or land use. Soil emissions of NO_x resulting from agricultural activities are included in the anthropogenic sector in the emission inventory of *Lamarque et al*. [2010]. Natural soil NO_x emissions are set to the PI value of 3.6 Tg N yr^{-1} following *Yienger and Levy* [1995] and are assumed to be constant in time. Lightning NO_x emissions in the model are calculated following *Horowitz et al*. [2003] as a function of subgrid convection parameterized in AM3 [*Donner et al*., 2011], resulting in a mean 1981–2000 total source of 4.5 ± 0.2 Tg N (as NO) per year with diurnal, seasonal, and interannual variability based on the model meteorology.

[15] Direct emissions of POA from biological activity in the ocean [*O'Dowd et al*., 2004] as a function of sea surface temperature and surface winds that vary with climate are also included. DMS emissions are calculated using an empirical function of prescribed fixed monthly mean DMS concentration in sea water and wind speed at 10 m, as described by *Chin et al*. [2002]. Dust emissions are parameterized following *Ginoux et al*. [2001], and sea salt particles are emitted

from the ocean according to *Monahan et al*. [1986]. Thus, emissions of oceanic POA and DMS, dust, and sea salt are dependent on the simulated meteorology in the model.

[16] Volcanic emissions implemented in the model are described by *Donner et al*. [2011]. Briefly, annual mean sulfur emissions (as SO_2) for continuous degassing and explosive volcanoes are from *Dentener et al*. [2006]. Given the large uncertainties in baseline volcanic emissions, these emissions are multiplied by a factor of 0.25, which is found to best match the observed SO_2 and sulfate concentrations in regions dominated by volcanic sources. Emissions from explosive volcanoes are injected 500 to 1500 m above volcano tops, while those from continuously degassing volcanoes are placed in the upper third of volcanoes. A time series of spatially distributed volcanic optical properties is imposed following *Stenchikov et al*. [2006] in the stratosphere to account for the lack of stratospheric aerosol microphysics.

[17] Global total emissions for years 1860 and 2000 are presented in Table 2. The global distribution of the absolute change in annual mean surface emissions of NO, CO, NMVOCs, black carbon, organic carbon, and SO_2 from 1860 to 2000 in Figure 1 shows that although global mean emissions increase (Table 2), emissions of some species decrease in some regions. For example, emissions of black carbon and organic carbon from the United States are lower in 2000 compared with 1860, driven by decreases in domestic fuel and biomass burning.

[18] Globally uniform concentrations of well-mixed greenhouse gases (WMGHGs), including carbon dioxide (CO_2), nitrous oxide (N_2O), CH_4, and ozone-depleting substances (ODSs including CFC-11, CFC-12, CFC-113, CCl_4, CH_3Cl, CH_3CCl_3, HCFC-22), are specified for radiation calculations from the Representative Concentration Pathways database (http://www.iiasa.ac.at/web-apps/tnt/RcpDb/) developed for climate model simulations for CMIP5 in support of IPCC-AR5 [*Meinshausen et al*., 2011]. Global mean concentrations of CH_4 and N_2O are specified at the surface as lower boundary conditions for chemistry. Tropospheric mixing ratios of halogen source gases are specified for the parameterization of the stratospheric source of Cl_y and Br_y.

2.4. Simulations

[19] We perform a base simulation of AM3 for the period 1980–2007 forced with interannually varying observed sea surface temperatures (SSTs) and sea ice cover (SIC) [*Rayner et al*., 2003], following the Atmospheric Model Intercomparison Project (AMIP) configuration. This simulation was forced with time-varying annual mean WMGHG and ODS concentrations, and short-lived pollutant emissions (with emissions for 1980–2000 from *Lamarque et al*. [2010] and post-2000 following the Representative Concentration Pathway 4.5 projection from *Lamarque et al*. [2011]). The short-lived pollutant emissions, provided at decadal increments (see section 2.3), are interpolated linearly for intermediate years within the model. The simulation was run for 28 years with the first year for initial spin-up. We analyze results from this simulation in section 3 to evaluate the capability of AM3 to simulate the atmospheric chemical composition.

[20] We perform two additional simulations of AM3 (Table 3) to investigate the impact of changes in emissions of short-lived species from PI to PD levels. These simulations follow the configuration designed by the Atmospheric Chemistry and Climate Model Intercomparison Project (ACCMIP) [*Lamarque et al*., 2013]. The "2000" simulation uses prescribed climatological monthly mean SST and SIC for the decade 1995–2004 taken from one ensemble member of the five-member ensemble historical simulation of the GFDL coupled model (GFDL CM3) conducted according to the CMIP5 specifications in support of the IPCC-AR5 [*John et al*., 2012; *Austin et al*., 2013]. Concentrations of WMGHGs, including CO_2, CH_4, N_2O, and ODSs, and emissions of short-lived pollutants (nonmethane ozone precursors and aerosols) are set to their year 2000 values. The "1860" simulation uses the same configuration, including the SST and SIC boundary conditions and WMGHG concentrations, except that short-lived pollutant emissions are set to their 1860 values as shown in Table 2 and surface concentrations of CH_4, a key ozone precursor [*West et al*., 2007], are set to their 1860 level (805 ppbv). CH_4 is held at its PD value (1751 ppbv) for radiation calculations in both the 1860 and the 2000 simulations; hence, any radiative flux changes between the 2000 and 1860 simulations result from forcing by ozone and aerosols and not by CH_4. Volcanic aerosols in the stratosphere are turned off in both these simulations. Emissions of all short-lived species, except dust, sea salt, DMS, and oceanic POA, do not include interannual variability in the 1860 and 2000 simulations as they are repeated over the run length. The dependence of dust, sea salt, DMS, and oceanic POA emissions on the simulated meteorology produces small differences in their emissions between the PD and PI (Table 2) simulations contributing to their burden changes, which are found to be statistically insignificant at 95% confidence level. To obtain a good signal-to-noise ratio, both simulations were run for 11 years with 1 year for spin-up.

[21] We compare results from the 1860 and 2000 simulations in section 4 to assess the impact of PI to PD changes in short-lived pollutant emissions and CH_4 burden on atmospheric composition and radiative forcing (only due to changes in ozone and aerosols). While the configuration with prescribed climatological SST and SIC is computationally efficient as opposed to running the full coupled model,

Table 3. Summary of AM3 Simulations

	Base (1981–2007)	2000	1860
CO_2	Time varying	2000	2000
CH_4	Time varying	2000	1860[a]
N_2O	Time varying	2000	2000
ODSs	Time varying	2000	2000
Sea surface temperature (SST)/sea ice cover (SIC)	Observed	1996–2005	1995–2004
Short-lived pollutant emissions	Time varying	2000	1860

[a]For radiation calculations, CH_4 was set to the 2000 level.

Table 4. Annual Mean Global Budget and Burdens Simulated by AM3[a]

	Annual Average (1981–2000) ± Standard Deviation	2000–1860
Tropospheric Ozone Budget		
Photochemical production[b] ($Tg\,yr^{-1}$)	5753 ± 244	2391 (69%)
Photochemical loss[c] ($Tg\,yr^{-1}$)	5019 ± 204	1948 (63%)
Net photochemical production ($Tg\,yr^{-1}$)	734 ± 44	444 (118%)
Dry deposition ($Tg\,yr^{-1}$)	1205 ± 20	505 (69%)
Cross-tropopause flux[d] ($Tg\,yr^{-1}$)	450 ± 26	53 (15%)
Ozone burden (Tg)	360 ± 7	103 (39%)
Global total column ozone (DU)	303 ± 5	16.9 (6%)
Tropospheric OH concentration(molec cm^{-3})	$1.05 \pm 0.02 \times 10^6$	-0.07×10^6 (−6.8%)
Tropospheric methane lifetime (yr)	8.5 ± 0.2	0.31 (3.6%)
Lightning NO_x emissions ($Tg\,N\,yr^{-1}$)	4.5 ± 0.2	−0.3 (−6.4%)
Tropospheric aerosol optical depth at 550 nm	0.16	0.05 (50.4%)
Global Total Burdens		
Carbon monoxide (Tg)	335 ± 11	158.4 (82%)
Tropospheric NO_x (Gg N)	195 ± 6.3	24.4 (14%)
Black carbon (Gg C)	126 ± 6.5	76 (140%)
Sulfate (Gg S)	572 ± 16.5	369 (206%)
Organic carbon (Gg C)	1776 ± 66	506 (40%)

[a]Average values and interannual standard deviations over the baseline 1981–2000 time period are shown in column 2. Effects of changing short-lived pollutant emissions and CH_4 concentration from 1860 to 2000 levels on global budget and burdens are shown in column 3 as absolute differences (2000–1860) and percent differences in parentheses.
[b]Calculated as the sum of all reactions of NO with peroxy radicals.
[c]Calculated as photochemical production minus net photochemical production.
[d]Includes advection, convection and vertical diffusion.

contrasting these simulations provides an estimate of the fast atmospheric responses, but not the slow feedbacks that involve ocean surface temperature changes [*Haywood et al*., 2009].

3. Model Evaluation

[22] We analyze mean results for the 1981–2000 time period from our base simulation, unless noted otherwise. The atmospheric physics and dynamics simulated in this model integration have been evaluated in detail by *Donner et al*. [2011]. In the following subsections, we focus on the evaluation of the simulated tropospheric ozone, CO, aerosols, and hydroxyl radical. We also compare with climatological aircraft observations of ozone, nitric oxide (NO), PAN, and propane (C_3H_8) [*Emmons et al*., 2000], noting that future work with targeted analyses of individual field campaigns should provide better insights into the source of model biases. Additionally, the photochemistry in AM3 has been evaluated in the context of the scientific questions addressed using the model (for example, ozone-temperature relationship [*Rasmussen et al*., 2012], transport of Asian pollution to surface air in the U.S. [*Lin et al*., 2012a], influence of strat-trop exchange on surface ozone [*Lin et al*., 2012b], and sensitivity of tropospheric oxidants to biomass burning emissions [*Mao et al*., 2013a]). Further, detailed evaluation of atmospheric composition simulated by AM3 has been performed within the ACCMIP effort [*Bowman et al*., 2013; *Lee et al*., 2013; *Naik et al*., 2013; *Shindell et al*., 2013; *Young et al*., 2013].

3.1. Ozone

[23] An annual global tropospheric (defined as the atmospheric domain in which annual mean ozone concentration is less than 150 ppbv) ozone burden of 360 Tg simulated by AM3 (Table 4) is within 10% of 335 ± 10 Tg derived from an observation-based ozone climatology [*Wild*, 2007, 2001]. The photochemical production and destruction of ozone are $5753 \pm 244\,Tg\,yr^{-1}$ and $5019 \pm 204\,Tg\,yr^{-1}$, respectively. Net photochemical production of $734 \pm 44\,Tg\,yr^{-1}$ in the troposphere exceeds the stratospheric influx (diagnosed in AM3 as the net dynamical flux across the tropopause) of $450 \pm 26\,Tg\,yr^{-1}$. Tropospheric loss by dry deposition at the surface accounts for $1205 \pm 20\,Tg\,yr^{-1}$. The simulated tropospheric ozone lifetime, calculated as the ratio of ozone burden and the total loss rate (photochemical loss plus surface deposition), is 21.1 days. A recent intercomparison of tropospheric ozone budget from 21 global models [*Stevenson et al*., 2006], mostly CTMs, estimates the mean tropospheric ozone production, loss, dry deposition, stratospheric influx (inferred as the residual of all other budget terms), and lifetime to be $5110 \pm 606\,Tg\,yr^{-1}$, $4668 \pm 727\,Tg\,yr^{-1}$, $1003 \pm 200\,Tg\,yr^{-1}$, $552 \pm 168\,Tg\,yr^{-1}$, and 22.3 days, respectively, for PD (year 2000), where the range is the multimodel standard deviation. The AM3 budget terms are within the range of these numbers, with the ozone production, loss, and dry deposition at the high end, while AM3 stratospheric flux is at the lower end of the multimodel mean. The global budget of tropospheric ozone simulated by AM3 is within the range of global PD tropospheric ozone budgets from modeling studies post-2000 [*Wu et al*., 2007], but the AM3 mean tropospheric ozone burden of 360 Tg is at the high end of the range (332 ± 30 Tg) of the more recent ACCMIP project [*Young et al*., 2013].

[24] We evaluate the simulated seasonal cycle of ozone in the lower stratosphere and troposphere by comparison with ozonesonde measurements made between 1995 and 2009. The observations are taken from the climatology described by *Tilmes et al*. [2012] built on previous work by *Logan* [1999]. Since the observed data are for 1995–2009, we compare the base simulation averaged over both 1981–2000 and 1995–2007 time periods (Figure 2) and find little difference in the AM3 ozone averaged over these separate periods, so we focus our evaluation on the 1995–2007 time period (shown in blue in Figure 2). At northern high-latitude sites

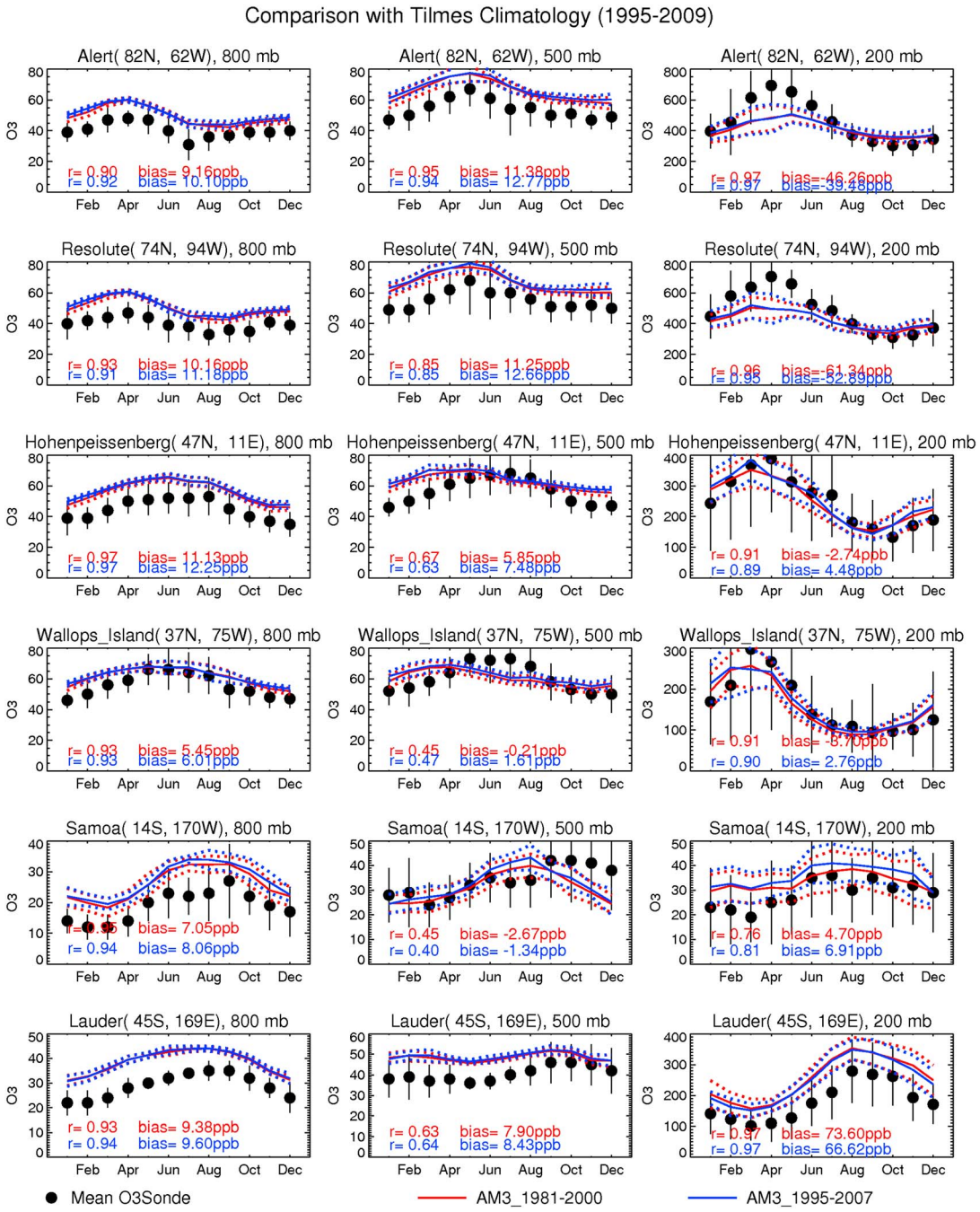

Figure 2. Comparison of simulated monthly mean ozone (ppbv) with observed ozonesonde climatology (black dots) for the period 1995 to 2009 at vertical levels of (left) 800 hPa, (middle) 500 hPa, and (right) 200 hPa. Vertical lines indicate standard deviation over the 1995–2009 time period. Solid lines indicate model ozone averaged for 1981–2000 (red) and 1995–2007 (blue) time periods, and dotted lines depict model standard deviation over these time periods.

(Alert and Resolute), AM3 reproduces much of the seasonal variation in ozone (correlation coefficient r calculated using monthly averaged observed and model data ranges between 0.8 and 0.9) for all vertical levels. The model overestimates the observed ozone concentrations by 9–13 ppbv in the lower (800 hPa) and middle (500 hPa) troposphere but underestimates observations by 40–50 ppbv in the upper troposphere (200 hPa). This low bias at 200 hPa is consistent with the underestimate of lower stratospheric ozone at northern high latitudes attributed to a deficiency in model transport [*Donner et al.*, 2011, Figure 7]. At northern midlatitudes (Hohenpeissenberg and Wallops Island), the observed seasonal cycle is represented well at 800 and 200 hPa ($r > 0.9$) but is too weak at 500 hPa. AM3 overestimates ozone concentrations at these sites by up to 12 ppbv with smaller biases in the middle and upper troposphere. The comparison is similar at Southern Hemisphere tropical (Samoa) and midlatitude (Lauder) stations: AM3 represents the ozone seasonal cycle

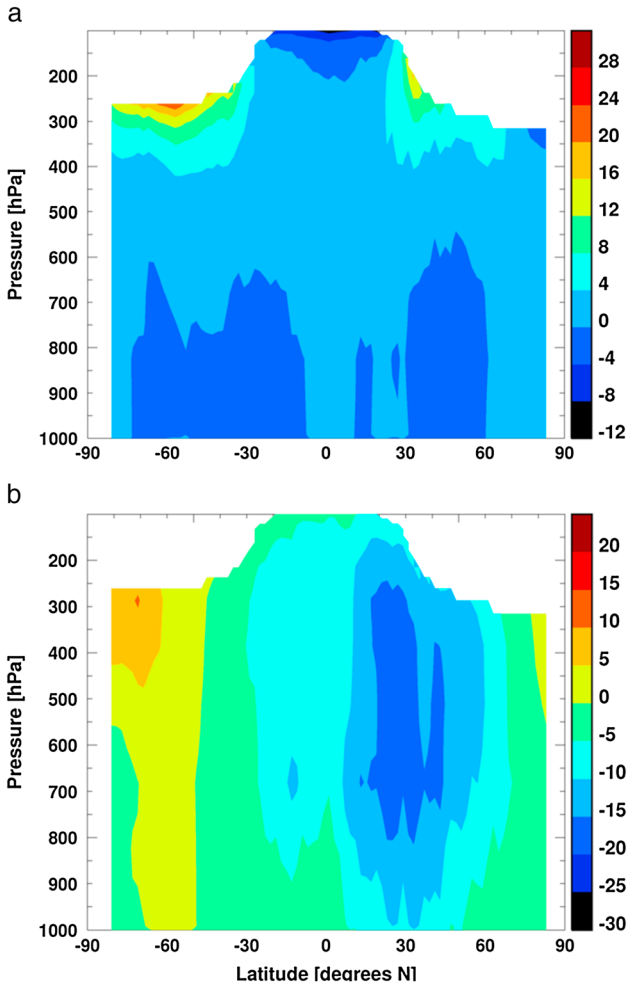

Figure 3. Zonal annual mean absolute bias of AM3 (a) ozone and (b) CO concentration relative to measurements by the Tropospheric Emission Spectrometer (TES) aboard the Aura satellite for the period 2005 to 2007 in the atmospheric domain where ozone concentration is less than 150 ppbv. Bias is calculated as AM3 minus TES in units of ppbv.

in the lower and upper troposphere ($r \sim 0.7$–0.9), while misrepresenting it in the midtroposphere (Figure 2). The simulated ozone concentrations are within 10 ppbv of the observations in much of the Southern Hemisphere, except AM3 overestimates by 67 pbbv the observations at 200 hPa over Lauder. The high bias in the upper troposphere over southern high latitudes reflects the overestimate of the observed lower stratospheric ozone concentrations as indicated by *Donner et al.* [2011].

[25] With the exception of a few locations, AM3-simulated ozone concentrations are within 10–15 ppbv of the observed values and reproduce the observed seasonal cycle, consistent with results from other chemistry-climate models [*Shindell et al.*, 2006a; *Lamarque et al.*, 2012]. Biases in AM3 ozone against ozonesonde measurements are similar across the current generation of CTMs and chemistry-climate models which consistently overestimate Northern Hemisphere tropospheric ozone concentrations [*Young et al.*, 2013].

[26] We compare the AM3 model zonal mean distribution of tropospheric ozone concentrations with the newly released version 5 [*Herman et al.*, 2011] ozone retrieved from the Tropospheric Emission Spectrometer (TES) instrument aboard the NASA-Aura satellite for the period 2005 to 2007 (Figure 3a). Extensive evaluation of a previous version of TES data against ozonesonde measurements shows that in general, TES has positive biases in the range of 3 to 10 ppbv throughout the troposphere [*Nassar et al.*, 2008]. Similar errors were found when TES version 5 was compared to the same set of ozonesondes that were used in the evaluation of earlier versions [*Herman et al.*, 2011]. We first interpolate the monthly mean AM3 ozone fields for 2005–2007 to TES pressure levels and then apply TES averaging kernels (AKs) and a priori matrix to account for differences in vertical resolution and the influence of clouds [*Kulawik et al.*, 2006]. *Aghedo et al.* [2011] show that applying the monthly mean TES AKs and a priori profiles to monthly mean model ozone produces negligible biases compared to convolving the simulated ozone with TES AKs each day at the overpass time. We show the difference between AM3 and TES within the troposphere in Figure 3a. We find that zonal mean distribution of AM3 ozone is within ± 4 ppb (−5% to 10%) for much of the lower to middle troposphere (surface—400 hPa) compared with TES observations (Figure 3a). In the upper troposphere high latitudes, the bias in the AM3 model ranges from 4 to 20 ppbv. Note that TES has an equally high bias in this region, due to decreased sensitivity, as found when TES ozone measured in October 2004 to October 2006 was evaluated against ozonesondes [*Nassar et al.*, 2008; *Herman et al.*, 2011]. Large biases in the upper troposphere where ozone has a greater radiative forcing efficiency [*Ramaswamy et al.*, 2001] could strongly influence the estimated radiative forcing from ozone changes.

[27] Additionally, we use aircraft observations of ozone, NO, PAN, and C_3H_8 from the *Emmons et al.* [2000] climatology to evaluate the AM3 distributions (Figure S1 in the supporting information). Generally, AM3 reproduces the observed vertical structure ozone in the observations (Figure S1a) and matches the observed mixing ratios to within one standard deviation, but has a tendency to overestimate the mixing ratios in the lower to middle troposphere, consistent with the comparison against ozonesonde data. Simulated NO values are generally within the range of the observed values throughout the troposphere (Figure S1b), although there is a slight tendency to underestimate values in the upper troposphere. The simulated PAN profiles agree with observations at most sites (Figure S1c); however, there are a few regions (e.g., the TRACE-A and SONEX regions) in which the model underestimates PAN concentrations throughout the troposphere, indicating either insufficient PAN precursors or inadequate transport in the model. AM3 underestimates observed concentrations of C_3H_8, a PAN precursor, in these same regions, likely suggesting a missing emission source in or upwind of these regions. Targeted analyses of individual observation campaigns with AM3 are needed to probe more deeply these model biases [e.g., *Horowitz et al.*, 2007; *Lin et al.*, 2012a, 2012b].

[28] We further evaluate the AM3-simulated surface ozone concentrations by comparison with data from surface observational networks in the United States (Clean Air Status and Trends Network—CASTNet http://www.epa.gov/castnet/) and Europe (European Monitoring and Evaluation Programme—EMEP http://www.nilu.no/projects/ccc/emepdata.html) and with published data from a few rural sites in India [*Naja and*

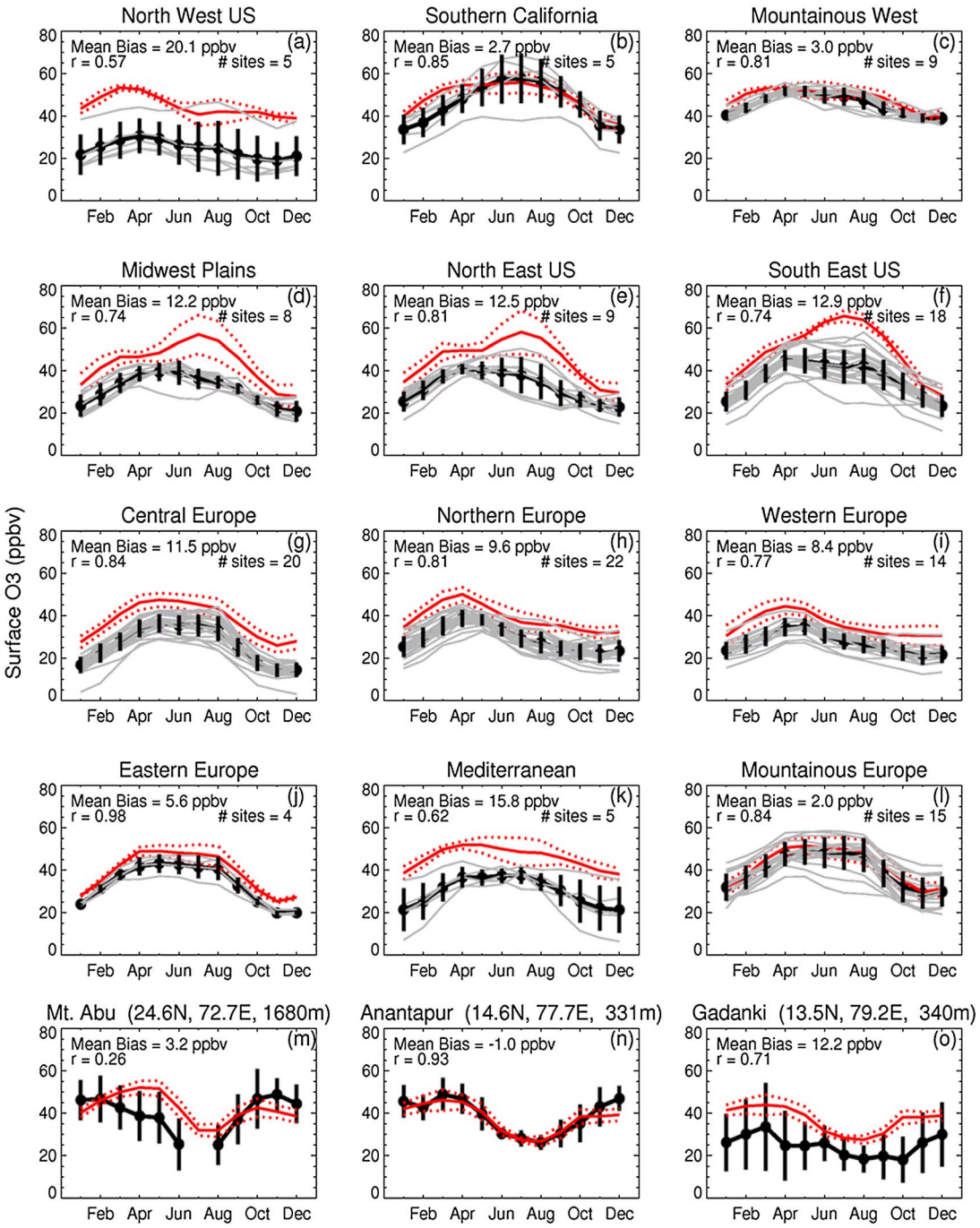

Figure 4. Comparison of AM3-simulated monthly mean surface ozone (ppbv) for 1981–2000 with measurements from CASTNet (http://www.epa.gov/castnet/) in the United States (1988–2009), EMEP (http://www.nilu.no/projects/ccc/emepdata.html) in Europe (1987–2008), and three sites in India. Black and red solid lines show the monthly mean observed and simulated surface ozone concentrations, respectively, averaged over all the sites falling within each region (defined in Table S1). Grey lines show ozone concentrations observed at each site included in the region. Vertical black and dotted red lines depict standard deviation in observed and simulated concentrations across the sites, respectively. For the Indian sites, vertical lines represent standard deviation in measurements.

Lal, 2002; *Naja et al*., 2003; *Reddy et al*., 2008]. Ozone measurements at CASTNet and EMEP sites, located in rural and remote areas with minimal urban influence, represent background ozone levels [*Tong and Mauzerall*, 2006; *Reidmiller et al*., 2009; *Henne et al*., 2010], thus making them ideal for evaluating a global model. We obtain climatological monthly means by averaging data over the total observational record at each station: 1988–2009 and 1987–2008 for CASTNet and EMEP, respectively. Based on geographical and topographical characteristics, we divide the U.S. and

Europe into six regions and average the data for sites that fall within each region (Table S1). Because of the limited number of observations available from India, we compare the model results with observations at each of the three individual sites. Surface ozone observations at Gadanki, Anantapur, and Mount Abu are for the periods 1993–1996 [*Naja and Lal*, 2002], 2002–2003 [*Reddy et al*., 2008], and 1993–2000 [*Naja et al*., 2003], respectively.

[29] AM3 broadly reproduces the observed mean seasonal cycle over all the regions of the United States and Europe ($r \sim 0.8$–0.9) (Figures 4a–4l). The model reproduces the observed ozone concentrations (biases within 3 ppbv) over high-altitude regions in both the United States and Europe (Figures 4c and 4l), an improvement over the underestimate by chemical-transport models found by *Fiore et al*. [2009]. At low-altitude sites, AM3 tends to be higher than the observations. In particular, the model overestimates observed surface ozone concentrations by 15–20 ppbv in the northwest United States (Figure 4a) and the Mediterranean (Figure 4k), where most sites are influenced by maritime air masses, suggesting an inadequate representation of chemistry and/or transport in the model. Mean ozone concentration biases are within 5 pbbv for Indian sites (Figures 4m–4o), except for Gadanki where it exceeds 10 ppbv. AM3 represents the observed seasonal cycle over Anantapur and Gadanki (Figures 4n and 4o) but misrepresents it over the high-altitude Mount Abu (Figure 4m). While the model simulates a seasonal cycle at Mount Abu that is typical of high-altitude sites with a springtime maximum due to downward transport from the free troposphere, the observed maximum ozone concentration in late autumn and winter has been attributed to the influence of cleaner marine air masses in spring [*Naja et al*., 2003].

[30] Overall, AM3 simulates the observed seasonal cycle and magnitude of surface ozone concentrations but has a tendency to overestimate Northern Hemisphere midlatitude concentrations. This overestimate is a common feature of the current generation of chemistry-transport models [*Fiore et al*., 2009] and chemistry-climate models [*Lamarque et al*., 2012]. Positive biases in AM3 ozone over the northern midlatitudes may be related to a combination of factors including emissions, excessive ozone production, and stratospheric intrusion in the model; treatment of isoprene nitrates [*Horowitz et al*., 2007; *Ito et al*., 2009]; underestimation of PAN dry deposition [*Wu et al*., 2012]; omission of halogen chemistry [*Parrella et al*., 2012]; or underestimation of aerosol reactive uptake of HO_2 [*Mao et al*., 2013b]. Carefully designed sensitivity AM3 simulations that take into account each of these factors will eventually provide more insight into model surface ozone biases.

3.2. Carbon Monoxide

[31] Next, we evaluate AM3 simulated CO mixing ratios near the surface against observed climatologies for 18 selected stations in the National Oceanic and Atmospheric Administration Environmental Science and Research Laboratory (NOAA ESRL) Carbon Cycle Cooperative Global Air Sampling Network [*Novelli and Masarie*, 2010]. Monthly mean data over the period 1988–2009 have been used to create a climatology for each station. AM3 is sampled at the grid box and altitude level corresponding to each station (Figure 5). In general, higher CO concentrations are observed in the Northern Hemisphere than in the Southern Hemisphere because of higher source strength in the Northern Hemisphere. The seasonal cycle at northern high and midlatitudes is strongly a function of photochemistry, with reduced OH abundance and weak vertical mixing resulting in accumulation of CO in the wintertime and increased OH leading to a significant decline in CO concentrations in summer. AM3 underestimates the seasonal variation in CO at all the northern high- and midlatitude sites considered here (Figures 5a–5f). The discrepancy is largest in late winter and spring when AM3 is biased low by 30–50 ppbv compared with the observations, similar to the multimodel biases discussed by *Shindell et al*. [2006b]. The negative biases could stem from high OH concentrations (see section 3.3 for a discussion of OH), the neglect of seasonality in anthropogenic CO emissions [*Shindell et al*., 2006b], or an underestimate of the total source of CO (direct and indirect from VOCs) in AM3.

[32] Observations show lower CO concentrations in the tropics than those at northern high and midlatitudes because of weaker emissions and more rapid loss. The observed seasonality in the tropics is governed by both anthropogenic and biomass burning emissions, with biomass burning emissions more important close to the equator and in the Southern Hemisphere tropics [*Novelli et al*., 1998; *Duncan et al*., 2007]. AM3 underestimates the seasonality and the magnitude of CO observed at most sites in the northern tropics (Figures 5h–5k). The observed springtime peak CO at Mauna Loa and Mariana Islands is attributed primarily to transport of pollution from Asia [*Brasseur et al*., 1996; *Jaffe et al*., 1997]. AM3 does not capture the springtime peak at these stations, indicating a possible problem with model transport and/or the magnitude of anthropogenic emissions from Asia. Mariana Islands is also influenced by dry season (spring) biomass burning in Southeast Asia [*Jaffe et al*., 1997], where springtime CO concentrations in AM3 are lower than those observed (Figure 5i), suggesting a problem with biomass burning emissions. AM3 reproduces the observed spring maximum at Christmas Island (Figure 5k) but simulates a second peak in fall, indicating a problem in the timing of biomass burning emissions. The seasonal cycle of biomass burning emissions in AM3 peaks 3 months too early over southern Africa as evidenced by the simulated CO versus observations at Ascension Island (Figure 5l), which receives biomass burning outflow from southern Africa [*Novelli et al*., 1998]. AM3 captures fairly well the seasonal cycle at subtropical sites in the Southern Hemisphere (Tutuila, Easter Island) sites, but is biased low. In the southern high and midlatitudes where CO concentrations are generally lower and the seasonality is determined by a combination of biomass burning emissions, oceanic emissions, and in situ hydrocarbon oxidation [*Holloway et al*., 2000], AM3 reasonably reproduces the observed magnitude and seasonal variation of CO (Figures 5o–5r).

[33] We also compare zonal mean AM3 tropospheric CO concentrations for 2005–2007 with those observed by TES (Figure 3b) following the same process of interpolation and application of TES operators (i.e., the TES averaging kernels and a priori matrix) as discussed in section 3.1. The patterns of global TES CO distributions in the troposphere have been found to agree with those from other satellites (e.g., MOPITT [*Luo et al*., 2007a; *Ho et al*., 2009]). TES CO profiles are also found to be within 10% of averaged in situ measurements [*Luo et al*., 2007b; *Lopez et al*., 2008]. AM3 underestimates

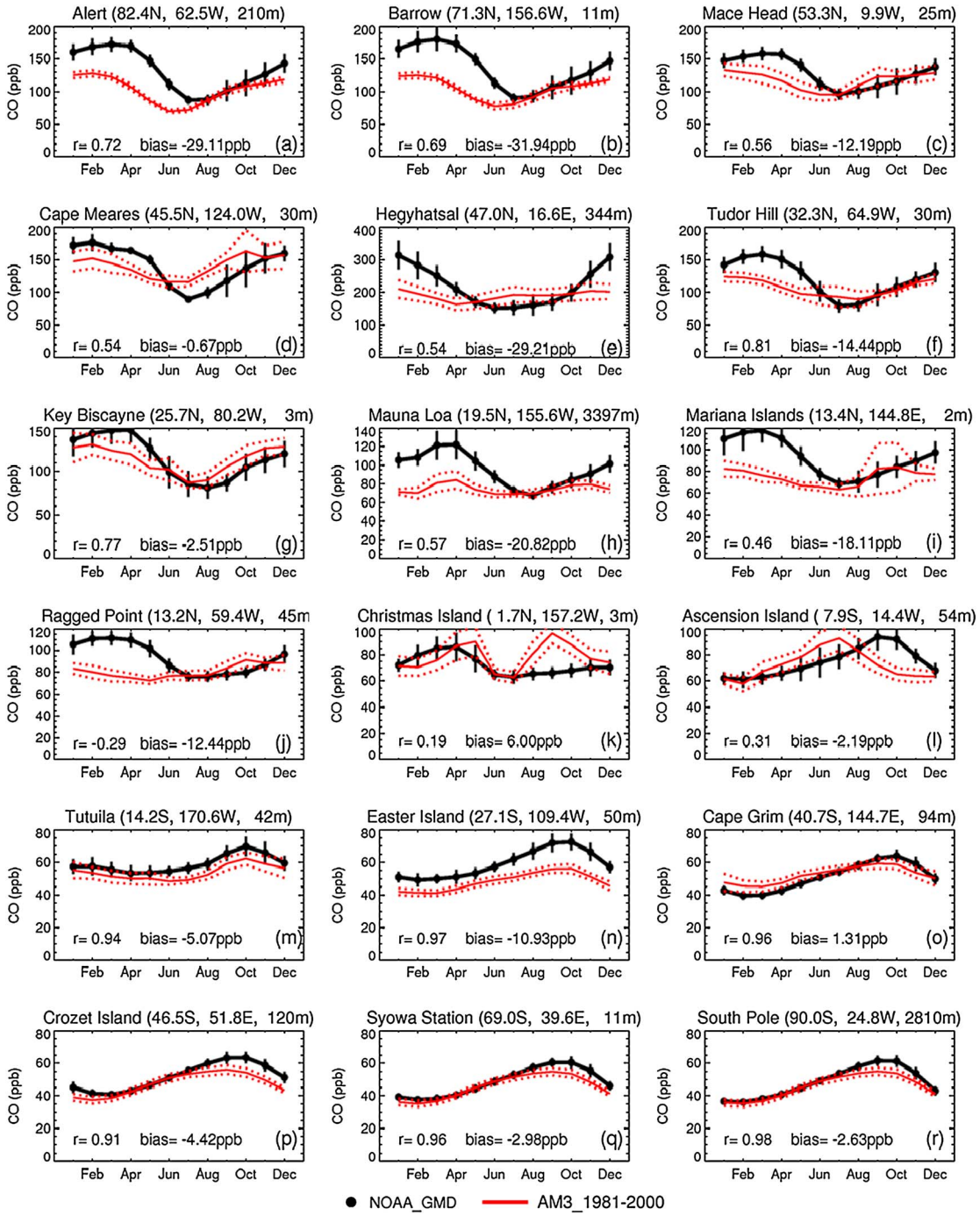

Figure 5. Comparison of model-simulated monthly mean (red) with observed CO concentrations (black) at surface sites. Observations are from *Novelli and Masarie* [2010] for the 1988 to 2010 period. Vertical black and red dotted lines represent the standard deviations of the observed and simulated concentrations, respectively, within each month.

the observed CO abundance by up to 20 ppbv in the northern extratropics throughout the troposphere and by ±10 ppbv in the southern troposphere. Elsewhere, the biases are negligible (less than ±5 ppbv). These results are also consistent with the comparison with surface CO measurements.

3.3. Aerosols

[34] Here, we evaluate AM3 simulated aerosol optical depth (AOD) against those retrieved from satellite measurements. Simulated AOD in our base run has been shown to be somewhat higher than ground-based Sun photometer measurements from the Aerosol Robotic Network, particularly over polluted regions [*Donner et al.*, 2011]. Figure 6 compares the evolution of AOD retrieved from the advanced very high resolution radiometer (AVHRR) over the ocean from 1982 to 2006 [*Geogdzhayev et al.*, 2002, 2004] with values from AM3. AM3 reproduces the enhancement, though with weaker amplitude, in total AOD after the eruptions of El Chichón (March

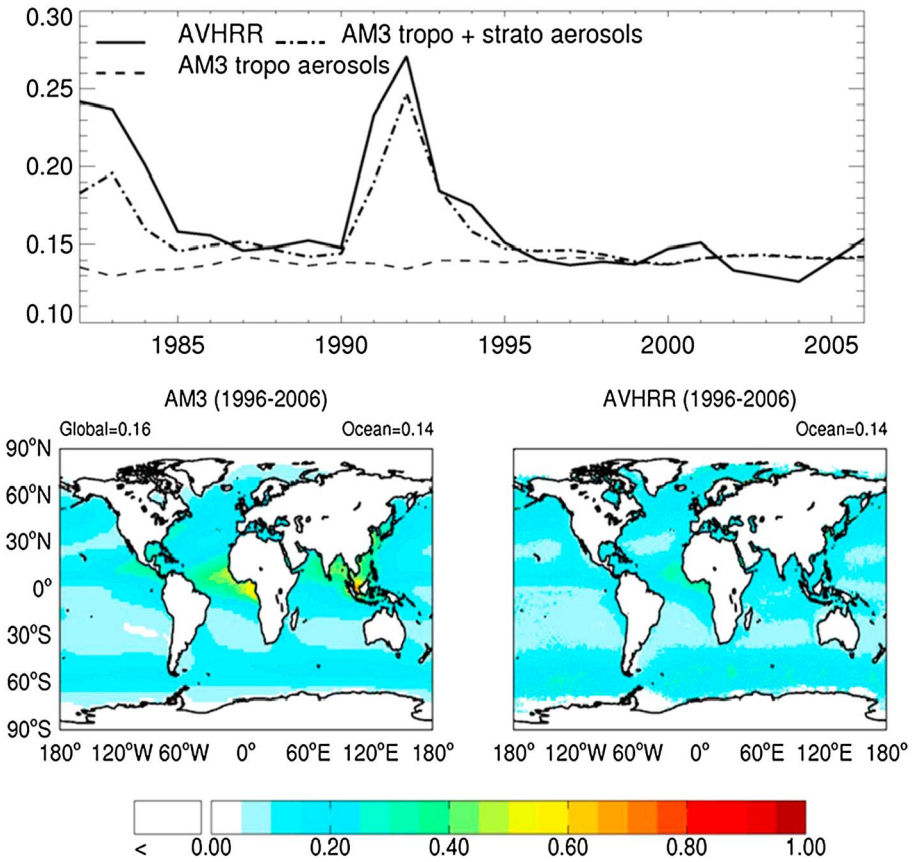

Figure 6. (top panel) Evolution of the global oceanic annual mean aerosol optical depth at 550 nm retrieved from AVHRR and that simulated by AM3 with tropospheric aerosols (dashed line) and with both tropospheric and volcanic aerosols (dash-dotted line) from 1982 to 2006. (bottom panel) Spatial distribution of annual mean oceanic aerosol optical depth at 550 nm averaged over the 1996 to 2006 time period (left) simulated by AM3 (tropospheric aerosols only) and (right) retrieved from AVHRR. Global and oceanic mean AOD simulated by AM3 is indicated on the left and right, respectively, and oceanic mean AOD observed by AVHRR is shown on the right on the bottom panels.

1982) and Mount Pinatubo (June 1991), followed by a slow decrease as aerosols are removed from the atmosphere. The mean bias of the AM3-simulated global AOD (tropospheric and stratospheric volcanic aerosols) versus the AVHRR observations is −5% over the 24 years with values ranging from −24% in 1982 to +12% in 2004. Over the 1996 to 2006 period, when the fraction of volcanic aerosols in the atmosphere is minimal, the mean bias is +2%. The good agreement at the global scale conceals biases on the regional scale as evident from the comparison of regional distribution of AOD from AM3 and AVHRRR (Figure 6, bottom panel) for the mean 1996–2006 period. AM3 overestimates the observed AOD in the northern midlatitude oceans and underestimates in the Southern Ocean. AM3 also overestimates observed AOD in the tropical and subtropical oceanic regions, particularly those influenced by biomass burning, likely resulting from errors in the biomass burning emissions implemented in the model. *Ginoux et al*. [2006] showed that in these regions, small bias of simulated relative humidity introduces large errors in AOD, when relative humidity is in excess of 90%.

3.4. Hydroxyl Radical and CH_4 Lifetime

[35] Hydroxyl radical (OH) determines the oxidizing capacity of the atmosphere, influencing the lifetime of many short-lived gaseous species [*Levy*, 1971]. The tropospheric OH concentration strongly depends on the atmospheric abundance of ozone, NO_x, CO, hydrocarbons, and water vapor and the distribution of solar radiation. Primary production of OH occurs when electronically excited $O(^1D)$ atom, produced by the photolysis of ozone, combines with water molecules [*Levy*, 1971; *Logan et al*., 1981; *Spivakovsky et al*., 2000]. Therefore, OH concentrations are highest in the tropical lower to middle troposphere, reflecting high levels of water vapor and ultraviolet radiation. Reaction with CO, CH_4, and NMVOCs, the dominant loss process of OH, produces peroxy radicals (HO_2 or RO_2) that can regenerate OH via reaction with NO and ozone [*Crutzen*, 1973]. This secondary production of OH via radical recycling by NO_x plays a more important role at higher latitudes where $O(^1D)$ and water vapor are less abundant [*Spivakovsky et al*., 2000; *Lelieveld et al*., 2002].

[36] Simulated global mean tropospheric OH concentrations can be tested against indirect estimates from observationally constrained budgets of species with known sources and reaction with OH as their primary sink, such as 1,1,1-trichloroethane (CH_3CCl_3, methyl chloroform), ^{14}CO, and $CHClF_2$ (HCFC-22) [*Spivakovsky et al*., 2000, and references therein]. The lifetime of CH_3CCl_3 derived from its

observed atmospheric abundances and known industrial emissions has most often been used to estimate the global mean abundance of OH [*Prinn et al*., 1995, 2001; *Krol et al*., 1998; *Krol and Lelieveld*, 2003; *Montzka et al*., 2000, 2011]. *Prinn et al*. [2001] estimate a global tropospheric mean CH_3CCl_3 lifetime of $5.99^{+0.95}_{-0.71}$ years for the period 1978–2000, while *Prather et al*. [2012] derive a value of 6.3 ± 0.4 years for 2010. Since AM3 does not simulate the chemistry of CH_3CCl_3, we assume a global uniform atmospheric mixing ratio to calculate its tropospheric lifetime as $\tau_{OH} = \frac{1}{\int_{sfc}^{trop} k(T)[OH]}$, where *k(T)*, the rate constant for the oxidation of CH_3CCl_3 by tropospheric OH, is 1.64×10^{-12} exp $(-1520/T)$ molecules^{-1} cm^3 s^{-1} [*Sander et al*., 2006]. Our estimated CH_3CCl_3 tropospheric mean lifetime of 5.3 ± 0.1 years over the period 1981–2000 is about 11% and 16% lower than the estimates of *Prinn et al*. [2001] and *Prather et al*. [2012], respectively; while within the uncertainty range, we conclude that AM3 OH is likely biased high.

[37] AM3 simulates a global mean air mass-weighted OH concentration of $(1.05 \pm 0.02) \times 10^6$ molecules cm^{-3} for the 1981–2000 period, with a Northern Hemisphere to Southern Hemisphere (NH/SH) ratio of 1.16 suggesting that higher concentrations of ozone, NO_x, and other OH precursors in the Northern Hemisphere dominate over the higher concentrations of CO, VOCs, and other sinks for OH in the model. While observational constraints on OH (more discussed below) indicate that the annual mean OH concentration is higher in the Southern Hemisphere than in the Northern Hemisphere (NH/SH < 1) [*Prinn et al*., 2001; *Montzka et al*., 2000; *Krol and Lelieveld*, 2003], most chemistry models [*Wang et al*., 1998; *Dalsøren and Isaksen*, 2006; *Naik et al*., 2013], including AM3, simulate higher Northern Hemisphere OH concentrations (NH/SH > 1). *Krol and Lelieveld* [2003] suggest that this discrepancy arises because the mean location of the Intertropical Convergence Zone (ITCZ), at 6°N [*Waliser and Gautier*, 1993], is used to determine the interhemispheric ratio from observations, implying that the amount of tropical air (with high OH) included in the Southern Hemisphere is larger than in the Northern Hemisphere. Models, on the other hand, assume that the hemispheres are symmetric around the equator. However, the ITCZ is used only in the analysis of *Montzka et al*. [2000], while *Prinn et al*. [2001] divide the hemispheres at the equator. Furthermore, observational estimates of the NH/SH OH ratio are highly uncertain as they rely on the assumption that the emission estimates and atmospheric observations of CH_3CCl_3 are accurate. Nevertheless, high OH concentrations in the Northern Hemisphere simulated by AM3 reflect the high ozone (section 3.1) and low CO biases (section 3.2) there.

[38] We compare the AM3 simulated air mass-weighted annual mean OH concentrations (Figure 7a) with the climatology of *Spivakovsky et al*. [2000] (Figure 7b) for 12 tropospheric subdomains as recommended by *Lawrence et al*. [2001]. AM3 simulates the highest boundary layer (surface to 750 hPa) OH burden in the tropics followed by the northern extratropics (30°N–90°N) and the southern extratropics (30°S–90°S), consistent with the climatology (Figure 7b), but is higher by about 25%–35%. AM3 OH concentrations decrease with increasing altitude as opposed to first decreasing in the midtroposphere and then increasing in the upper troposphere as in the *Spivakovsky et al*. [2000] climatology. The vertical OH distribution in AM3 is, however, similar to that of other chemistry-climate models [*Folberth et al*., 2006; *Jöckel et al*., 2006; *Lamarque et al*., 2012]. Excessive OH in the tropical boundary layer could indicate limitations in our treatment of higher volatile organic compounds [*Mao et al*., 2009]. For example, AM3 does not include representation of higher (five and more carbon atoms) alkanes, alkenes, and aromatic compounds, thus reducing the OH sink (for example, the MOZART-4 mechanism which includes higher NMVOC yields an OH vertical distribution that better matches the climatology [*Emmons et al*., 2010]). Furthermore, differences in the AM3-simulated and climatological OH distributions could also indicate deficiencies in the meteorology simulated by AM3 (e.g., water vapor biases).

[39] AM3 simulates a mean total atmospheric CH_4 burden of 4622 Tg and tropospheric CH_4 loss by reaction with OH of 540 Tg yr^{-1}, resulting in mean tropospheric CH_4 lifetime against loss by tropospheric OH of 8.6 years, about 10% lower than the lifetime of 9.6 years reported by *Prather et al*. [2001]. It is within the range of values (7.8–10.5 years) simulated by other models [*Lawrence et al*., 2001; *Folberth et al*., 2006; *Jöckel et al*., 2006; *Fiore et al*., 2009; *Emmons et al*., 2010; *Lamarque et al*., 2012] and a recent multimodel mean estimate of 9.7 ± 1.5 years [*Naik et al*., 2013]. Including a nominal stratospheric sink of 40 Tg yr^{-1} and a soil sink of 30 Tg yr^{-1} yields a global atmospheric CH_4 lifetime of 7.6 years, on the low side of the 8.7 ± 1.3 and 8.6 ± 1.2 years from multimodel estimates of *Stevenson et al*. [2006] and *Voulgarakis et al*. [2013], respectively, and an observation-based estimate of 9.1 ± 0.9 years [*Prather et al*., 2012].

4. Impact of Short-Lived Pollutants on Composition and Climate

[40] In this section, we compare 10 year annual mean fields from 2000 and 1860 simulations to investigate the impact of changes in short-lived pollutants (emissions of precursors of ozone and aerosols and CH_4 concentrations) from PI to PD levels on atmospheric composition (section 4.1) and climate forcing (section 4.2).

4.1. Impact on Atmospheric Composition

4.1.1. Ozone

[41] We simulate a 39% increase in the annual mean global tropospheric ozone burden from 263 Tg in PI to 365 Tg in the PD (Table 4). Of the total 103 Tg increase in tropospheric ozone burden, 62% occurs in the Northern Hemisphere, consistent with the much larger NO_x emission increase in the Northern Hemisphere (Figure 1). The photochemical production and loss of ozone increase by 69% and 63%, respectively. The deposition flux of ozone increases by 69% in response to the increased ozone burden. The (photochemical and depositional) lifetime of ozone decreases from 25 days in the PI to 21 days in the PD simulation. In addition, the cross-tropopause flux, diagnosed in AM3 as the net dynamical ozone flux, is 15% greater in the PD relative to the PI simulation. The global average ozone column increases by about 16.9 Dobson unit (DU) with tropospheric and stratospheric increases of 9.4 DU (39%) and 7.5 DU (2%), respectively.

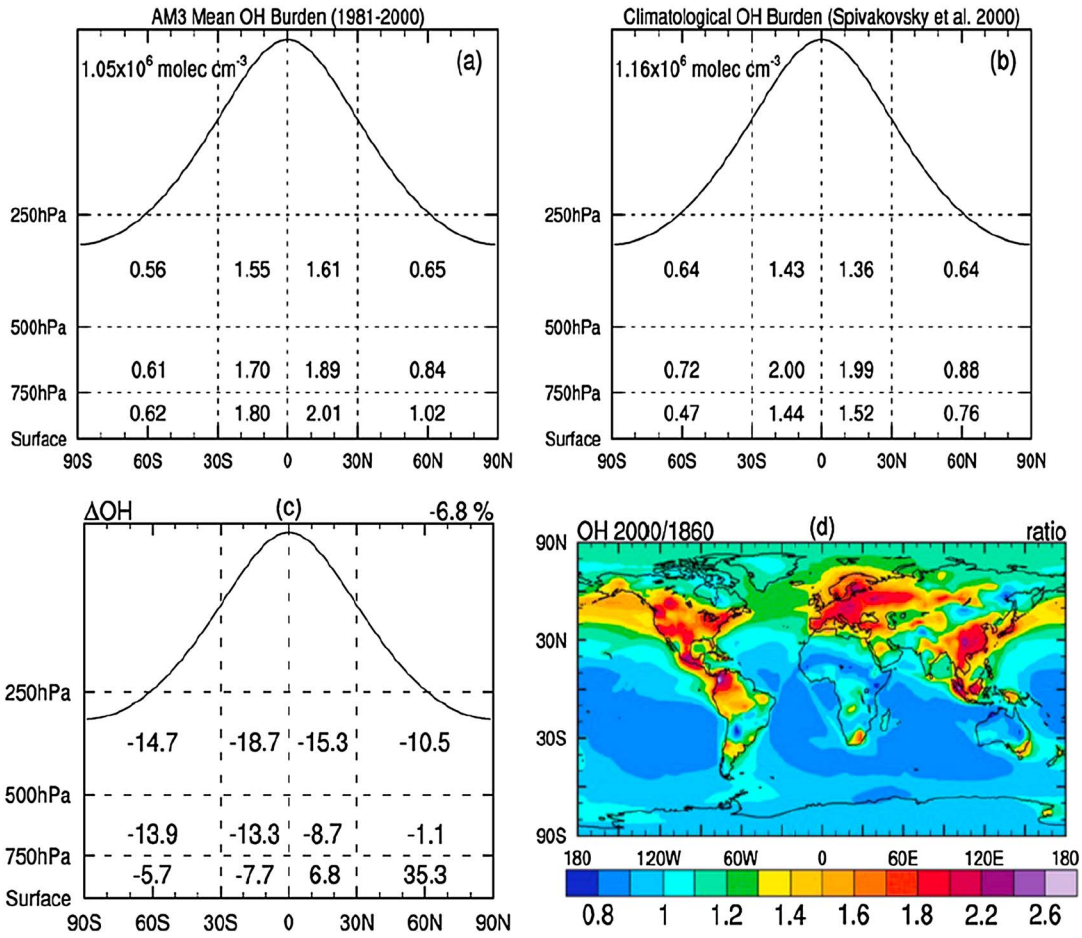

Figure 7. (a) Annual mean OH burden from AM3 compared with the (b) climatological mean of *Spivakovsky et al*. [2000], (c) percent change in air mass-weighted mean OH concentrations in various subdomains of the atmosphere in response to short-lived pollutant emission and CH_4 concentration changes from PI to PD (2000–1860), and (d) ratio of mean surface to 750 hPa OH in the 2000 and 1860 simulations.

[42] With ODSs held constant at their PD values for both the 2000 and 1860 simulations, the small increase (2%) in stratospheric ozone occurs via changes in CH_4 concentrations. Increasing CH_4 increases water vapor in the upper stratosphere and mesosphere, enhancing the loss of ozone catalyzed by the HO_x radicals ($HO_x = H + HO_2 + OH$). In the lower stratosphere, however, the CH_4 increase causes ozone to increase via NO_x-induced ozone production [*Wayne*, 1991; *Brasseur and Solomon*, 1986] just as in the troposphere. Further, increases in CH_4 also act to reduce the chlorine-catalyzed destruction of ozone by converting chlorine atoms to the reservoir hydrochloric acid (HCl; $CH_4 + Cl \rightarrow HCl + CH_3$) in the lower stratosphere [*Wayne*, 1991; *Fleming et al*., 2011]. Thus, the overall consequence is a 2% increase in stratospheric ozone in the 2000 simulation relative to that in 1860.

[43] Total annual column ozone is simulated to increase by 25–35 DU over the industrialized areas of the Northern Hemisphere (Figure 8a). Global annual average surface ozone concentrations increase by ~14 ppbv from PI to PD, with largest increases over regions coinciding with the largest increases of precursor emissions (Figure 8b). The interhemispheric asymmetry (NH/SH) in surface ozone concentrations increases from 1.1 in PI to 1.4 at PD (the distribution of simulated surface ozone concentrations for PI and PD is shown in Figure S2). Greater NO_x emission increases in the Northern Hemisphere aided by CH_4 increases (globally uniform) produce more ozone in the Northern Hemisphere, thus contributing to the enhanced interhemispheric asymmetry in surface ozone in the PD relative to PI.

[44] Our simulated tropospheric ozone burden increase of 103 Tg in response to changes in short-lived pollutants is within the range (71–140 Tg) of previously published tropospheric ozone increase from PI to PD [*Lamarque et al*., 2005b, and references therein]. It is also within the range of more recent estimates of PI to PD ozone increases from *Liao and Seinfeld* [2005] (128 Tg), *Horowitz* [2006] (113 Tg), *Shindell et al*. [2006a] (41 Tg), *Lamarque et al*. [2010] (99 Tg), *Skeie et al*. [2011] (108 Tg), and *Young et al*. [2013] (multimodel mean ozone increase of 88 Tg).

4.1.2. CO and NO_x

[45] The global annual mean CO burden increases by 82% (Table 4) in response to PI to PD changes in the anthropogenic and biomass burning emissions of CO and NMVOC, and CH_4 concentrations. Near-homogenous increases in CO burden are simulated (Figure 8c), except for strong source regions, for example, the biomass burning areas of Southeast

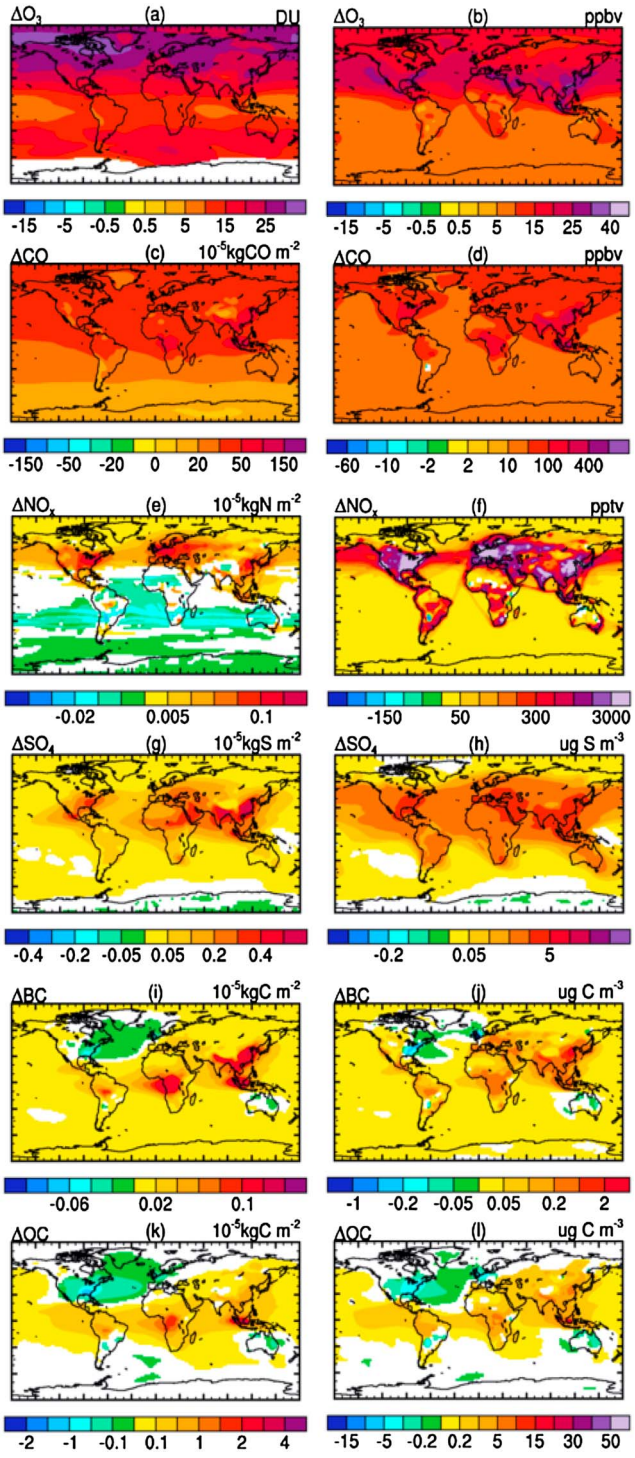

Figure 8. AM3-simulated changes in (left panel) column burden and (right panel) surface concentrations of (a, b) ozone (O_3), (c, d) CO, (e, f) tropospheric NO_x, (g, h) sulfate ($SO_4^=$), (i, j) black carbon (BC), and (k, l) organic carbon (OC) in response to short-lived pollutant emission and CH_4 concentration changes from PI to PD (2000–1860). Units for each variable plotted are shown on the top right corner. Areas where change is insignificant ($p = 95\%$ Student's t test) are not colored.

Asia and Central Africa, and anthropogenic emissions areas of North America, China and South Asia. Increases in zonal average CO concentrations extend from the surface to the tropopause, with increases of 30 to 60 ppb in the Northern Hemisphere and 10 to 20 ppb in the Southern Hemisphere (not shown). Surface CO concentrations increase by up to 400 ppb locally over source regions (Figure 8d).

[46] The annual mean tropospheric NO_x burden increases by 14% in the PD relative to PI (Table 4), with maximum increases near source regions in the Northern Hemisphere (Figure 8e). Small decreases in the NO_x burden in the Southern Hemisphere are attributed to the simulated decrease in lightning NO_x emissions over the Southern Hemisphere extratropical land areas (Figure S3). NO_x emissions from lightning, the main source of NO_x in the free troposphere, especially in the PI, decrease in the PD by about 6% (statistically significant at 95% confidence level; Table 4), consistent with a 7% decrease in global lightning frequency (Figure S3). Previous modeling studies have shown that lightning activity and the resulting NO_x emissions will increase in a warmer climate [e.g., *Price and Rind*, 1994; *Reeve and Toumi*, 1999; *Shindell et al*., 2006a]; however, we do not see this response in our experiments as our PD and PI simulations use fixed SST. Large uncertainties exist in the modeling of long-term changes in convection, lightning [*Tost et al*., 2007; *Williams*, 2009], and consequently lightning NO_x emissions [*Schumann and Huntrieser*, 2007, and references therein].

[47] Annual mean surface NO_x concentrations increase by up to 3 ppbv over the northeastern US, Europe, northern India, and China source regions (Figure 8f), following the PI to PD increases in emissions (Figure 1). Surface NO_x also increases over oceanic ship tracks; however, this increase may be overestimated as plume processes are not accounted for our global model [*Lamarque et al*., 2010]. With a lifetime of a day, most NO_x increases are confined near the surface, as opposed to the CO increases that are more homogenous throughout the troposphere.

4.1.3. Aerosols

[48] Simulated global burdens of sulfate, black carbon, and organic carbon increase by factors of 3, 2.4, and 1.4 from PI to PD (Table 4), within the range of previous published estimates [*Horowitz*, 2006; *Stier et al*., 2006; *Tsigaridis et al*., 2006; *Lamarque et al*., 2010]. Our simulated changes in global aerosol burden are significantly lower than those simulated by *Horowitz* [2006], in part because of differences in the applied emissions. *Horowitz* [2006] set PI (1860) anthropogenic emissions of aerosols and their precursors to zero and biomass burning emissions, specifically those from biofuel, savannah, tropical forest, and agricultural waste burning (not extratropical forests), to 10% of PD (1990) levels. Thus, *Horowitz* [2006] applied factors of 75, 12, and 6 increases in the surface emissions of SO_2, BC, and OC, respectively, significantly higher than the factors of 20, 2, and 1.2 applied in this study. Historical emissions of short-lived pollutants are highly uncertain [*Lamarque et al*., 2010], thus making it difficult to accurately estimate the historical changes in aerosol burden.

[49] The largest increases in sulfate aerosol column occur in the equator to 30°N latitude band (Figure 8g), a region which is characterized by high emissions and oxidation capacity. The atmospheric burden of sulfate aerosols depends on sources (SO_2 emissions, level of atmospheric oxidants,

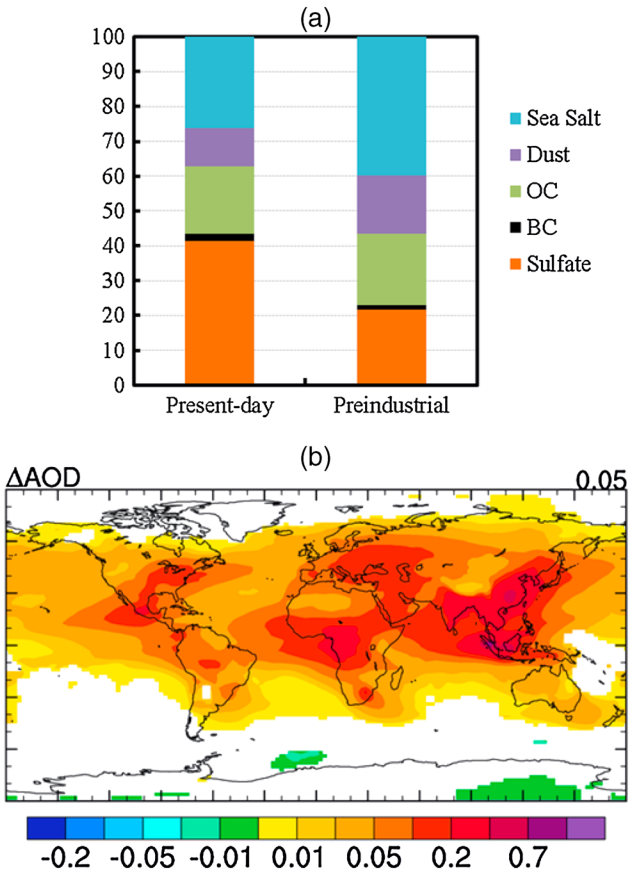

Figure 9. (a) Contribution of each aerosol species simulated by AM3 to the global annual mean AOD for PD (2000) and PI (1860), and (b) change in annual mean aerosol optical depth (AOD) at 550 nm in response to short-lived pollutant emission and CH_4 concentration changes from PI to PD; global mean value is indicated on the top right of the plot.

including ozone, OH, NO_3^-, and H_2O_2) and sinks (wet and dry deposition). Higher PD versus PI SO_2 emissions lead to increased formation of sulfate aerosols in the PD simulation. At the surface, sulfate concentrations increase by up to 15 $\mu g\,S\,m^{-3}$ (Figure 8h) in regions of high SO_2 emissions (Asia, Europe, and North America). Secondary maxima in the increase of surface sulfate concentrations occur in the Southern Hemisphere over regions of high biomass burning (South America, Africa, and Southeast Asia).

[50] The atmospheric burden of carbonaceous aerosols is governed by their emissions and deposition (wet and dry). Black carbon emissions are driven by human activities that involve combustion of mostly fossil fuels with smaller contributions from domestic biofuel burning and biomass burning, while organic carbon emissions predominantly come from the latter two categories. Because of the large natural background source of organic carbon, increase in its global fractional burden is smaller than that for black carbon. Reduced PD emissions from domestic biofuel burning and forest clearing in midlatitude regions (North America, Europe, and Australia) drive decreases in carbonaceous aerosol burden over these regions (Figures 8i and 8k). Conversely, sharp increases are simulated for regions with high PD emissions (China, India, central Africa). Changes in the burden are dominated by changes near the surface (Figures 8j and 8l). Simulated PD surface concentrations are lower than PI over most of North America, Europe, and Australia but exceed PI values in highly populated areas of Asia, Eastern Europe, and central Africa (Figures 8j and 8l).

[51] The global mean AOD at 550 nm increases by 50% from a PI value of 0.10 to a PD value of 0.15 (Table 4). The largest increase in AOD comes from sulfate, followed by the increase in black carbon and organic carbon, respectively (Figure 9a). Further, the relative contribution of sulfate and black carbon to AOD almost doubles from PI to PD, in response to increases in their atmospheric loading (Table 4). Spatially, the largest increases in AOD from PI to PD (Figure 9b) coincide with regions of largest increases in anthropogenic emissions (Figure 1). Our estimate of the PI to PD change in AOD is in qualitative agreement with the 21% increase simulated by *Tsigaridis et al.* [2006].

4.1.4. Tropospheric OH

[52] Next, we investigate the changes in tropospheric oxidizing capacity resulting from PI to PD changes in short-lived pollutant emissions and increases in CH_4 concentration. The tropospheric mean air mass-weighted OH concentration decreases by about 7% (Table 4) in response to PI to PD changes in short-lived pollutants, suggesting that increases in OH sinks (CH_4 burden and emissions of CO, SO_2, and NMVOCs) dominate over increases in sources (tropospheric ozone, water vapor, and NO_x emissions) in the model. The OH decrease acts to increase the tropospheric lifetime of CH_4 by about 4% (Table 4). When we compare our 2000 simulation with a sensitivity simulation (not shown) in which we set the emissions of NO_x, CO, NMVOCs, and aerosols (or their precursors) to 1860 levels but CH_4 to PD levels, we find that tropospheric mean OH increases by 10% as a result of increasing emissions alone. This suggests that CH_4 plays a dominant role in controlling global mean OH changes over long time scales.

[53] Regionally, OH decreases in all regions of the atmosphere except in the lower (surface to 750 hPa) Northern Hemisphere, with the largest increase (35%) occurring in the lower extratropical troposphere (Figure 7c), coinciding with the largest increases in OH sources—NO_x and ozone. Figure 7d shows the spatial distribution of the increase in OH in the lowest atmospheric subdomain (surface to 750 hPa) where more than 60% of the total oxidation of CH_4 occurs [*Lawrence et al.*, 2001]. OH increases by almost a factor of 2 over Northern Hemisphere regions with high PD NO_x emissions and ozone concentrations. OH decreases in the Southern Hemisphere are attributed to increases in CH_4, which is more important as an OH sink in the Southern Hemisphere than in the Northern Hemisphere [*Spivakovsky et al.*, 2000].

[54] Large uncertainties exist in the estimates of PI to PD changes in tropospheric OH. Previous modeling estimates of PI to PD changes in tropospheric mean OH abundance range from increases of 6%–15% to decreases of 5%–33% [see *John et al.*, 2012, Table 1]. Applying transient PI to PD simulations (with time-varying WMGHG and ODS concentrations, and short-lived pollutant emissions) of the fully coupled chemistry-climate model, GFDL CM3, *John et al.* [2012] find a 6% decrease in tropospheric mean OH concentrations. Using results from ACCMIP models, *Naik et al.* [2013] find that the multimodel mean tropospheric

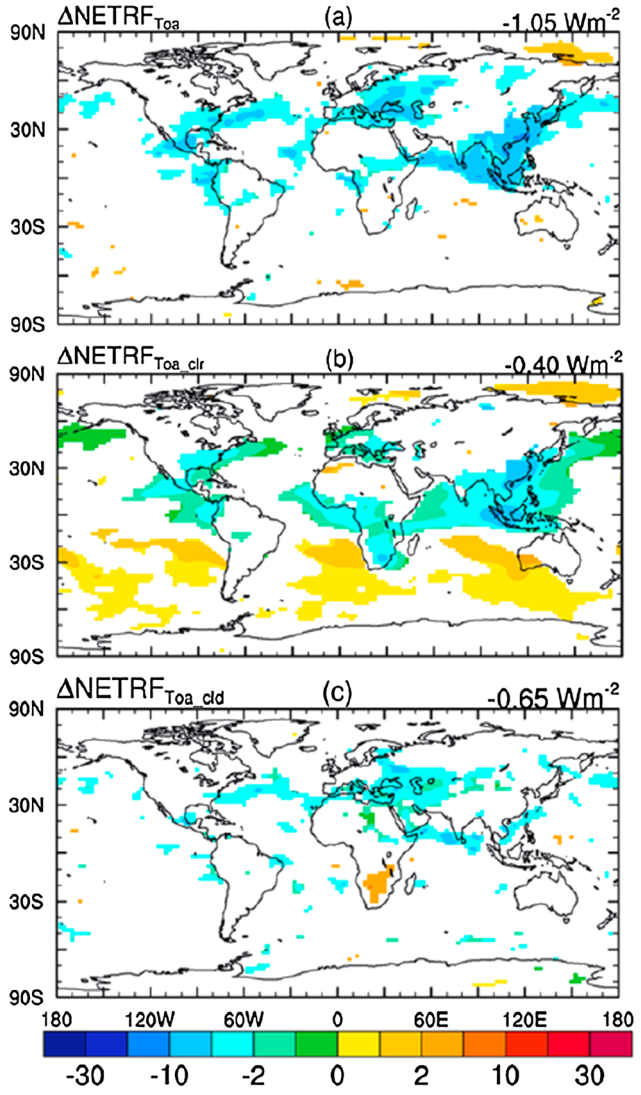

Figure 10. Net annual mean top-of-the-atmosphere (a) all-sky radiative perturbation flux (RFP), (b) clear-sky RFP, and (c) cloudy-sky RFP, due to changes in short-lived pollutant emissions from PI to PD. Global mean values are indicated at the top right of each plot. Areas where change is insignificant ($p = 95\%$ Student's t test) are not colored.

OH abundance has remained nearly constant over the past 150 years. Our estimate of changes in OH concentrations resulting from PI to PD changes in short-lived pollutant emissions and CH_4 concentrations falls within the range of these previous estimates.

4.2. Impact on Radiative Forcing and Climate

[55] To investigate the potential for changes in short-lived pollutant emissions from PI to PD to influence climate, we assess here the net adjusted radiative forcing from these emission changes. Note that we expect the climate responses to be weak in our experiments, which are conducted with fixed SST and SIC. We calculate the radiative forcing due to combined changes in ozone and aerosols (from emission changes) as the change in the net irradiance (shortwave plus longwave) at the top of the atmosphere (TOA) with fixed ocean conditions, but allowing for rapid adjustments to the climate system (including atmospheric temperatures and clouds). Since our PD and PI simulations use fixed SST and SIC extent, our calculated TOA radiative forcing, more appropriately referred to as "radiative flux perturbation" (RFP) or "fixed-SST" forcing, incorporates the effects of fast atmospheric responses to short-lived pollutants but not the slow feedbacks associated with changes in global ocean temperatures [*Hansen et al.*, 2005; *Forster et al.*, 2007; *Haywood et al.*, 2009; *Lohmann et al.*, 2010]. RFP at the TOA has been shown to predict the global mean surface temperature change that will result from changes in short-lived pollutants [*Hansen et al.*, 2005; *Forster et al.*, 2007; *Lohmann et al.*, 2010]. While useful, we do not diagnose the contribution of individual short-lived climate forcers to the net RFP here. RFPs due to historical changes in individual short-lived climate forcers as simulated by the GFDL AM3 are briefly discussed by *Levy et al.* [2013] and are fully described by Horowitz et al. (in preparation, 2013).

[56] The net global annual average all-sky TOA RFP due to ozone and aerosols resulting from PI to PD changes in short-lived pollutant emissions and CH_4 concentrations is $-1.05\ \mathrm{W\,m^{-2}}$ in our model, implying a net radiative cooling of the climate system from PI to PD changes in ozone and aerosols. Tropospheric ozone increases produce a positive forcing, while aerosol increases exert either a positive forcing (black carbon) or a negative forcing (sulfate, organic carbon) on the climate system. Aerosols also produce a negative indirect forcing via changes in cloud optical properties or a positive forcing from changes in the thermal structure of the atmosphere. Our results indicate that the strong negative forcing (direct plus indirect) from PI to PD aerosol changes dominates over the positive forcing due to ozone increases and aerosol semidirect effect. Our net ozone and aerosol RFP of $-1.05\ \mathrm{W\,m^{-2}}$ is comparable to the multimodel mean (eight models) PI to PD aerosol plus ozone forcing of $-0.84 \pm 0.50\ \mathrm{W\,m^{-2}}$ [*Shindell et al.*, 2013, Table 8]. Further, our net ozone and aerosol RFP offsets nearly half of the positive radiative forcing of $2.30 \pm 0.23\ \mathrm{W\,m^{-2}}$ from PI to PD changes in WMGHGs calculated by *Shindell et al.* [2013], indicating that on a global scale, short-lived pollutants have acted to mask a portion of the anthropogenic greenhouse gas forcing. Thus, future reductions in short-lived pollutant emissions for health reasons will likely unmask the warming due to long-lived greenhouse gases [*Levy et al.*, 2013].

[57] Figure 10a shows the geographical distribution of the annual mean all-sky TOA RFP due to PI to PD short-lived pollutant emissions. The largest statistically significant negative RFPs (up to $-10\ \mathrm{W\,m^{-2}}$) are simulated over industrialized regions of the Northern Hemisphere characterized by high aerosol burdens (China, India, Europe, North America). Smaller negative RFPs are also simulated for regions where biomass burning emissions increased over the last century, such as Southeast Asia, central Africa, and parts of the Amazon, and over oceans downwind of source regions. The simulated forcing over much of the globe is statistically insignificant relative to the model internal variability, possibly because 10 year runs are too short to produce a robust signal that can be distinguished from noise [*Golaz et al.*, 2011].

[58] To explore the role of changes in cloud properties on radiative forcing, we break down the all-sky RFP to

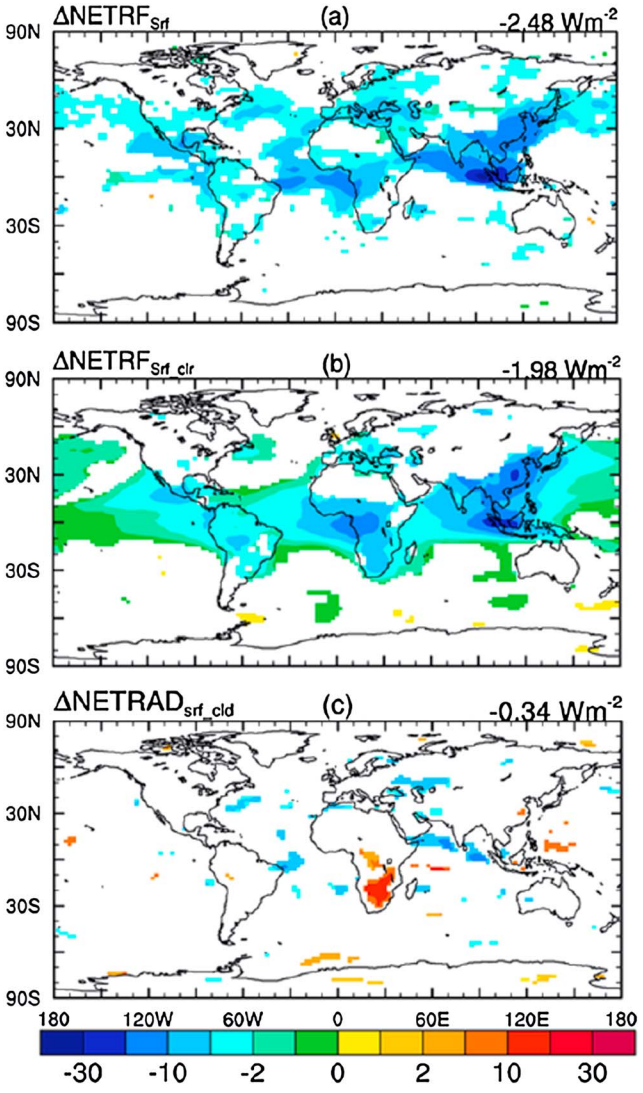

Figure 11. Net annual mean surface (a) all-sky radiative perturbation flux (RFP), (b) clear-sky RFP, and (c) cloudy-sky RFP, due to changes in short-lived pollutant emissions from PI to PD. Global mean values are indicated at the top right of each plot. Areas where change is insignificant (p = 95% Student's t test) are not colored.

clear-sky and cloudy-sky components. Clear-sky radiative fluxes (shortwave and longwave) are calculated by diagnostic calls to the radiation code in the model including the aerosol absorption and scattering but excluding cloud absorption and scattering; thus, these fluxes do not include changes from aerosol indirect effects and cloud modifications via direct aerosol interactions [*Golaz et al.*, 2011]. We diagnose the cloudy-sky RFP (includes aerosol indirect effects and cloud modifications via direct aerosol interactions) by taking the difference between all- and clear-sky RFPs. Figures 10b and 10c show the spatial distribution of the clear-sky and cloudy-sky RFPs. From a global mean perspective, both the clear and cloudy sky RFPs are negative and the contribution of the cloudy sky RFP ($-0.65\ \mathrm{W\,m^{-2}}$) is slightly higher than that of clear-sky RFP ($-0.40\ \mathrm{W\,m^{-2}}$) to the all-sky RFP, suggesting that aerosol indirect effects and direct cloud modifications contribute strongly to the net ozone plus aerosol forcing. Spatially, negative RFPs over and downwind of industrialized areas in the Northern Hemisphere, and biomass burning regions persist in the clear-sky component (Figure 10b), suggesting the dominance of reflecting aerosols (sulfate and organic) over absorbing aerosols (black carbon) and tropospheric ozone.

[59] Next, we analyze the RFP at the surface, as observational evidence indicates that aerosols affect the surface energy budget and hydrological cycle [*Ruckstuhl et al.*, 2008; *Philipona et al.*, 2009]. PI to PD change in short-lived pollutant emissions results in a global mean all-sky surface RFP of $-2.5\ \mathrm{W\,m^{-2}}$, implying that the emission changes result in an additional $1.5\ \mathrm{W\,m^{-2}}$ absorbed by the atmosphere. The geographical distribution of all-sky surface RFP (Figure 11a) is similar to that of the TOA RFP but with enhanced negative forcing (up to $-20\ \mathrm{W\,m^{-2}}$) over industrialized regions and biomass burning area characterized by large aerosol burden changes, and neighboring oceans. The clear-sky component of the surface RFP (Figure 11b) dominates over the cloudy-sky component (Figure 11c). Previous studies have indicated that aerosols have a stronger impact on precipitation than well-mixed greenhouse gases because the former can effectively alter the surface shortwave flux available for evaporation [*Feichter et al.*, 2004; *Lohmann and Feichter*, 2005; *Ming and Ramaswamy*, 2009]. Consistent with the negative surface forcing, we find that the global mean precipitation diminishes by $0.03\ \mathrm{mm\,yr^{-1}}$; however, much of the spatial distribution of the precipitation change is statistically insignificant (not shown).

5. Discussion and Conclusions

[60] We have documented and evaluated atmospheric chemistry in the newly developed GFDL chemistry-climate model AM3 (section 3) and applied the model to investigate the net impact of short-lived air pollutant emission changes from preindustrial (PI) to present day (PD) on atmospheric composition and climate forcing (section 4). Comparison of our base simulation (1980–2007 with interannually varying SSTs and SIC) with observations suggests that AM3 is able to reproduce the observed tropospheric ozone (ozone) seasonal cycle (Pearson correlation coefficient r = 0.45–0.97) and simulated concentrations are within 10 to 15 ppbv of observed values. Surface carbon monoxide (CO) concentrations are biased low in late winter and spring compared with observations at all northern high- and midlatitude sites similar to the multimodel biases discussed in *Shindell et al.* [2006b], but the observed seasonality (r = 0.91–0.96) and magnitude are captured at Southern Hemisphere middle and high latitudes. Tropospheric CO concentrations for 2005–2007 in our base simulation are within 15% of those observed by the TES satellite. Global mean aerosol optical depth agrees well with that observed by the AVHRR satellite over the 1982–2006 time period; however, there are regional differences of opposite signs. Hydroxyl radical (OH), the primary determinant of the tropospheric lifetime of many short-lived pollutants, is somewhat higher in our base simulation than in the climatological estimates, consistent with the high ozone and low CO biases in our model. Consistent with high OH, our mean tropospheric methane (CH_4) lifetime is 8.6 years, on the lower side of published values.

[61] Contrasting the atmospheric composition in our PI (1860) and PD (2000) simulations, both with fixed PD sea surface temperature, sea ice extent, and WMGHG concentrations, shows substantial increases in the PD global total burdens of tropospheric ozone, sulfate, and carbonaceous aerosols relative to PI driven by short-lived pollutant emission and CH_4 concentration changes. Spatially, surface ozone increases everywhere, more so in the Northern Hemisphere than in the Southern Hemisphere, mostly driven by increases in NO_x emissions. Spatially inhomogeneous changes in aerosol burdens result from the different regional trends in their emissions. For example, carbonaceous aerosol burdens over North America and Europe decrease from the PI to the PD because of reduced domestic fuel burning. Uncertainties in short-lived pollutant emissions will influence our estimate of the historical changes in the abundance of ozone and aerosols. *Lamarque et al*. [2010] note that uncertainties in regional emissions can be larger than a factor of 2.

[62] We simulate a 7% decrease in tropospheric air mass-weighted OH concentration in response to PI to PD changes in emissions and CH_4 burden, indicating that increases in OH sinks (CH_4, CO, NMVOCs, and SO_2) dominate over OH sources (ozone and NO_x). Consequently, CH_4 lifetime increases by 4% for the PD relative to PI. Analysis of our fully coupled climate-chemistry atmosphere-ocean model (GFDL CM3) simulations with short-lived pollutant emissions and greenhouse gas concentrations, including CH_4, evolving over the entire historical period shows that CH_4 lifetime increases from PI to PD, demonstrating the dominant impact of CH_4 on its own lifetime [*John et al*., 2012]. Although we consider the direct influence of aerosols on gases via heterogeneous chemistry, we do not include their impact on photolysis rates, previously shown to increase the CH_4 lifetime by decreasing tropospheric OH [*Bian et al*., 2003]. In addition, we did not consider stratospheric ozone depletion resulting from PI to PD increases in ODSs, which could modulate the changes in tropospheric ozone and aerosol burden, oxidizing capacity, and therefore CH_4 lifetime. The impacts from historical changes in ODS should be considered to estimate more completely the full anthropogenic influence on the chemistry-climate system over the last century.

[63] We analyze radiative forcing at the top-of-the-atmosphere (TOA), expressed as radiative flux perturbation, to estimate that substantial anthropogenic increases in tropospheric ozone and aerosol burden in the PD relative to PI cause a strong negative forcing ($-1.05\,W\,m^{-2}$). This finding suggests that the negative forcing (direct plus indirect) from aerosol changes dominates over the positive forcing due to ozone increases and aerosol semidirect effect, thus masking nearly half of the historical long-lived greenhouse gas forcing globally. Statistically significant negative TOA forcing is concentrated over industrialized regions of the Northern Hemisphere characterized by high sulfate aerosol burden changes (China, India, Europe, and North America). Negative forcing is enhanced at the surface and is more widespread compared with the TOA forcing.

[64] Our estimate of the TOA forcing from short-lived pollutants may be compared with other estimates obtained using the *Lamarque et al*. [2010] emission inventory applied here. For example, our TOA RFP for ozone and aerosol RFP of $-1.05\,W\,m^{-2}$ is comparable to the multimodel mean (eight models including AM3) PI to PD aerosol plus ozone forcing of $-0.84 \pm 0.50\,W\,m^{-2}$ [*Shindell et al*., 2013, Table 8]. *Bauer and Menon* [2012] used this emission inventory to calculate a TOA forcing of $-0.6\,W\,m^{-2}$ for PI to PD changes in aerosol (or aerosol precursor) emissions only. Our stronger negative TOA forcing compared with that of *Bauer and Menon* [2012] could be attributed to differences in model configuration (their model included only the cloud albedo effect of aerosols). Similar experiments with other chemistry-climate models will help to determine whether this net impact of short-lived pollutants on climate forcing since the PI period is robust. Finally, here we have assessed only the fast responses due to changes in short-lived pollutant emissions; however, the ocean is likely to respond to these forcings on a longer time scale. Analysis of simulations of the GFDL coupled ocean-climate-chemistry model (CM3) with evolving sea surface temperature and sea ice extent indicates that over the historical period (2000–1860), aerosol and aerosol precursor emission changes only result in 1.0°C of global cooling [*Levy et al*., 2013]. Warming induced by historical changes in tropospheric ozone, not considered by *Levy et al*. [2013], will likely dampen the cooling effect of aerosols in CM3 (Horowitz et al., in preparation, 2013).

Appendix A

[65] The total rate of wet deposition (W, in units of mixing ratio s^{-1}) for a gaseous species is given by

$$W = \left(\Gamma^{incv,ls} + \Gamma^{ls}_{bc} \right) \cdot C,$$

where C (mixing ratio) is the local concentration of the gas, $\Gamma^{cv,ls}_{in}$ (s^{-1}) is the in-cloud scavenging coefficient for large-scale and convective precipitation, and Γ^{ls}_{bc} (s^{-1}) is the below-cloud scavenging coefficient for large-scale precipitation. The in-cloud scavenging coefficient for soluble gases is

$$\Gamma^{cv,ls}_{in} = 1 - e^{(-\beta \cdot f)}; \beta = \frac{P^{k+1}_{\text{rain}} - P^{k}_{\text{rain}} + P^{k+1}_{\text{snow}} - P^{k}_{\text{snow}}}{\Delta p \cdot g^{-1} \cdot \chi_{\text{liq}}},$$

where f is the scavenging factor or the fraction of gas incorporated in cloud condensate as determined by Henry's law equilibrium [*Donner et al*., 2011], $P^{k+1} - P^{k}$ ($kg\,m^{-2}\,s^{-1}$) is the precipitation flux generated in layer k, Δp (Pa) is the pressure thickness of the model layer k, g ($m\,s^{-2}$) is the gravitational acceleration, and χ_{liq} ($= \frac{\text{cloud water (kg)}}{\text{air mass (kg)}}$) is the liquid water content calculated by the large-scale and convective cloud parameterizations. In-cloud wet removal for convective precipitation is computed only within the updraft plumes and mesoscale anvils. In-cloud scavenging is also considered for aerosols following the same scheme but with prescribed values of scavenging factor (f) [*Donner et al*., 2011; *Fang et al*., 2011].

[66] Below-cloud scavenging of gases for large-scale precipitation is computed as

$$\Gamma^{ls}_{bc} = K_g \left(c_g - c_{g*} \right),$$

where $K_g = \frac{D_g}{d} \left[2 + 0.6 \sqrt{\left(\frac{d w_D}{\nu}\right)} \sqrt[3]{\frac{\nu}{D_g}} \right]$ ($m\,s^{-1}$) is the gas-phase mass transfer coefficient; c_g and c_{g*} (mixing ratio) are the concentrations of the species in gas phase and at the surface

of the rain drop, respectively; the diffusive coefficient $D_g = 1.12e{-}5\ \mathrm{m^2\,s^{-1}}$; the mean diameter of rain drop $d = 1.89e{-}3\ \mathrm{m}$; the rain drop terminal velocity $w_D = 7.48\ \mathrm{m\,s^{-1}}$; and the kinematic viscosity of air $v = 6.18e{-}6\ \mathrm{m^2\,s^{-1}}$. Re-evaporation of falling precipitation (where $P^{k+1} - P^k < 0$) returns dissolved species to the atmosphere as in *Liu et al.* [2001]. Below-cloud washout of aerosols for large-scale precipitation is parameterized as by *Li et al.* [2008] and *Fang et al.* [2011].

[67] **Acknowledgments.** We are grateful to Simone Tilmes and Martin Schultz for kindly providing the ozonesonde data and surface ozone analysis package, respectively. We thank Yuanyuan Fang, Issac Held, Jasmin John, Meiyun Lin, Yi Ming, and V. Ramaswamy for useful discussions. We appreciate helpful suggestions from Songmiao Fan on an earlier version of this manuscript. Comments from four anonymous reviewers helped to significantly improve this manuscript.

References

Aghedo, A. M., K. W. Bowman, D. T. Shindell, and G. Faluvegi (2011), The impact of orbital sampling, monthly averaging and vertical resolution on climate chemistry model evaluation with satellite observations, *Atmos. Chem. Phys.*, *11*, 6,493–6,514.

Austin, J., and J. Wilson (2010), Sensitivity of polar ozone to sea surface temperatures and halogen amounts, *J. Geophys. Res.*, *115*, D18303, doi:10.1029/2009JD013292.

Austin, J., L. W. Horowitz, M. D. Schwarzkopf, R. J. Wilson, and H. Levy II (2013), Stratospheric ozone and temperature simulated from the preindustrial era to present day, *J. Climate*, *26*, 3,528–3,543, doi:10.1175/JCLI-D-12-00162.1.

Bauer, S. E., and S. Menon (2012), Aerosol direct, indirect, semidirect, and surface albedo effects from sector contributions based on the IPCC AR5 emissions for preindustrial and present-day conditions, *J. Geophys. Res.*, *117*, D01206, doi:10.1029/2011JD016816.

Bauer, S. E., D. Koch, N. Unger, S. M. Metzger, D. T. Shindell, and D. G. Streets (2007), Nitrate aerosols today and in 2030: A global simulation including aerosols and tropospheric ozone, *Atmos. Chem. Phys.*, *7*, 5,043–5,059, doi:10.5194/acp-7-5043-2007.

Bellouin, N., J. Rae, A. Jones, C. Johnson, J. Haywood, and O. Boucher (2011), Aerosol forcing in the Climate Model Intercomparison Project (CMIP5) simulations by HadGEM2-ES and the role of ammonium nitrate, *J. Geophys. Res.*, *116*, D20206, doi:10.1029/2011JD016074.

Bey, I., D. J. Jacob, R. M. Yantosca, J. A. Logan, B. Field, A. M. Fiore, Q. Li, H. Liu, L. J. Mickley, and M. Schultz (2001), Global modeling of tropospheric chemistry with assimilated meteorology: Model description and evaluation, *J. Geophys. Res.*, *106*, 23,073–23,096.

Bian, H., M. J. Prather, and T. Takemura (2003), Tropospheric aerosol impacts on trace gas budgets through photolysis, *J. Geophys. Res.*, *108*, 4242, doi:10.1029/2002JD002743.

Bowman, et al. (2013), Evaluation of ACCMIP outgoing longwave radiation from tropospheric ozone using TES satellite observations, *Atmos. Chem. Phys.*, *13*, 4057–4072, doi:10.5194/acp-13-4057-2013.

Brasseur, G. P., and S. Solomon (1986), *Aeronomy of the Middle Atmosphere*, 2nd edn., 644pp, Dordrecht, The Netherlands.

Brasseur, G. P., D. A. Hauglustaine, and S. Walters (1996), Chemical compounds in the remote Pacific troposphere: Comparison between MLOPEX measurements and chemical transport model calculations, *J. Geophys. Res.*, *101*, 14,795–14,813.

Brasseur, G. P., D. A. Hauglustaine, S. Walters, P. J. Rasch, J.-F. Müller, C. Granier, and X. X. Tie (1998), MOZART, a global chemical transport model for ozone and related tracers: 1. Model description, *J. Geophys. Res.*, *103*, 28,265–28,289.

Carslaw, K. S., B. P. Luo, and T. Peter (1995), An analytic expression for the composition of aqueous HNO_3-H_2SO_4 stratospheric aerosols including gas phase removal of HNO_3, *Geophys. Res. Lett.*, *22*, 1,877–1,880, doi:10.1029/95GL01668.

Chin, M., P. Ginoux, S. Kinne, O. Torres, B. N. Holben, D. N. Duncan, R. V. Martin, J. A. Logan, A. Higurashi, and T. Nakajima (2002), Tropospheric aerosol optical depth from the GOCART model and comparisons with satellite and Sun photometer measurements, *J. Atmos. Sci.*, *59*, 461–483.

Crutzen, P. J. (1973), A discussion of the chemistry of some minor constituents in the stratosphere and troposphere, *Pure Appl. Geophys.*, *106–108*, 1,385–1,399.

Dalsøren, S. B., and I. S. A. Isaksen (2006), CTM study of changes in tropospheric hydroxyl distribution 1990–2001 and its impact on methane, *Geophys. Res. Lett.*, *33*, L23811, doi:10.1029/2006GL027295.

Delworth, T. L., et al. (2006), GFDL's CM2 global coupled climate models. Part I: Formulation and simulation characteristics, *J. Climate*, *19*(5), doi:10.1175/JCLI3629.1.

Dentener, F., et al. (2006), Emissions of primary aerosol and precursor gases in the years 2000 and 1750 prescribed datasets for AeroCom, *Atmos. Chem. Phys.*, *6*, 4,321–4,344.

Donner, L. J., et al. (2011), The dynamical core, physical parameterizations, and basic simulation characteristics of the atmospheric component of the GFDL global coupled model CM3, *J. Climate*, *24*, 3,484–3,519, doi:10.1175/2011JCLI3955.

Duncan, B., J. A. Logan, I. Bey, I. A. Megretskaia, R. M. Yantosca, P. C. Novelli, N. B. Jones, and C. P. Rinsland (2007), Global budget of CO, 1988–1997: Source estimates and validation with a global model, *J. Geophys. Res.*, *112*, D22301, doi:10.1029/2007JD008459.

Emmons, L. K., D. A. Hauglustaine, J.-F. Müller, M. A. Carroll, G. P. Brasseur, D. Brunner, J. Stahelin, V. Thouret, and A. Marenco (2000), Data composites of airborne observations of tropospheric ozone and its precursors, *J. Geophys. Res.*, *105*, 20,497–20,538.

Emmons, L. K., et al. (2010), Description and evaluation of the Model for Ozone and Related chemical Tracers, version 4 (MOZART-4), *Geosci. Model Dev.*, *3*, 43–67.

Eyring, V., I. S. A. Isaksen, T. Berntsen, W. J. Collins, J. J. Corbett, O. Endresen, R. G. Grainger, J. Moldanova, H. Schlager, and D. S. Stevenson (2009), Transport impacts on atmosphere and climate: Shipping, *Atmos. Environ.*, doi:10.1026/j.atmosenv.2009.04.059.

Fang, Y., A. M. Fiore, L. W. Horowitz, A. Gnanadesikan, I. Held, G. Chen, G. Vecchi, and H. Levy (2011), The impacts of changing transport and precipitation on pollutant distributions in a future climate, *J. Geophys. Res.*, *116*, D18303, doi:10.1029/2011JD015642.

Feichter, J., E. Roeckner, U. Lohmann, and B. Leipert (2004), Nonlinear aspects of the climate response to greenhouse gas and aerosol forcing, *J. Clim.*, *17*, 2,384–2,398.

Fiore, A. M., D. J. Jacob, B. D. Field, D. G. Streets, S. D. Fernandes, and C. Jang (2002), Linking air pollution and climate change: The case for controlling methane, *Geophys. Res. Lett.*, *29*(19), 1919, doi:10.1029/2002GL015601.

Fiore, A. M., et al. (2009), Multimodel estimates of intercontinental source-receptor relationships for ozone pollution, *J. Geophys. Res.*, *114*, D04301, doi:10.1029/2008JD010816.

Fleming, E. L., C. H. Jackman, R. S. Stolarksi, and A. R. Douglass (2011), A model study of the impact of source gas changes on the stratosphere for 1850–2100, *Atmos. Chem. Phys.*, *11*, 8,515–8,541.

Folberth, G. A., D. A. Hauglustaine, J. Lathière, and F. Brocheton (2006), Interactive chemistry in the Laboratoire de Mètèorologie Dynamique general circulation model: Model description and impact analysis of biogenic hydrocarbons on tropospheric chemistry, *Atmos. Chem. Phys.*, *6*, 2,273–2,319.

Forster, P., et al. (2007), Changes in atmospheric constituents and in radiative forcing, in *Climate Change 2007: The Physical Science Basis. Contribution of Working Group I to the Fourth Assessment Report of the Intergovernmental Panel on Climate Change*, edited by S. Solomon et al., pp. 129–234, Cambridge Univ. Press, Cambridge, U. K.

Fuglestvedt, J. S., T. K. Berntsen, I. S. A. Isaksen, H. Mao, X.-Z. Liang, and W.-C. Wang (1999), Climatic forcing of nitrogen oxides through the changes in tropospheric ozone and methane: Global 3D model studies, *Atmos. Environ.*, *33*, 961–977.

Geogdzhayev, I. V., M. I. Mishchenko, W. B. Rossow, B. Cairns, and A. A. Lacis (2002), Global two-channel AVHRR retrievals of aerosol properties over the ocean for the period of NOAA-9 observations and preliminary retrievals using NOAA-7 and NOAA-11 data, *J. Atmos. Sci.*, *59*, 262–278.

Geogdzhayev, I. V., M. I. Mishchenko, L. Liu, and L. Remer (2004), Global two-channel AVHRR aerosol climatology: Effects of stratospheric aerosols and preliminary comparisons with MODIS and MISR retrievals, *J. Quant. Spectrosc. Radiat. Transfer*, *88*, 47–59.

GFDL Global Atmospheric Model Development Team (2004), The new GFDL global atmosphere and land model AM2-LM2: Evaluation with prescribed SST simulations, *J. Clim.*, *17*, 4,641–4,673.

Ginoux, P., M. Chin, I. Tegen, J. M. Prospero, B. Holben, O. Dubovik, and S.-J. Lin (2001), Sources and distributions of dust aerosols simulated with the GOCART model, *J. Geophys. Res.*, *106*, 22 255–22 274.

Ginoux, P., L. W. Horowitz, V. Ramaswamy, I. V. Geogdzhayev, B. N. Holben, G. Stenchikov, and X. Tie (2006), Evaluation of aerosol distribution and optical depth in the Geophysical Fluid Dynamics Laboratory coupled model CM2.1 for present climate, *J. Geophys. Res.*, *111*, D22210, doi:10.1029/2005JD006707.

Giorgi, F., and W. L. Chameides (1985), The rainout parameterization in a photochemical model, *J. Geophys. Res.*, *90*, 7,872–7,880.

Golaz, J.-C., M. Salzmann, L. J. Donner, L. W. Horowitz, Y. Ming, and M. Zhao (2011), Sensitivity of the aerosol indirect effect to subgrid

variability in the cloud parameterization of the GFDL Atmosphere General Circulation Model AM3, *J. Climate*, *24*(13), doi:10.1175/2010JCLI3945.1.

Granier, C., J. F. Lamarque, A. Mieville, J. F. Muller, J. Olivier, J. Orlando, J. Peters, G. Petron, G. Tyndall, and S. Wallens (2005), POET, a database of surface emissions of ozone precursors, available at: http://www.aero.jussieu.fr/projet/ACCENT/POET.php, 2005.

Griffies, S. M., et al. (2011), The GFDL CM3 coupled climate model: Characteristics of the ocean and sea ice simulations, *J. Clim.*, *24*, doi:10.1175/2011JCLI3964.1.

Hansen, J., et al. (2005), Efficacy of climate forcings, *J. Geophys. Res.*, *110*, D18104, doi:10.1029/2005JD005776.

Hanson, D. R., and K. Mauersberger (1988), Laboratory studies of nitric acid trihydrate: Implications for the south polar stratosphere, *Geophys. Res. Lett.*, *15*, 855–858.

Haywood, J., L. Donner, A. Jones, and J.-C. Golaz (2009), Global indirect radiative forcing caused by aerosols: IPCC (2007) and beyond, in *Clouds in the Perturbed Climate System: Their Relationship to Energy Balance, Atmospheric Dynamics, and Precipitation*, edited by J. Heintzenberg, and R. J. Charlson, pp. 451–567, MIT Press, Cambridge.

Henderson, S. C., and U. K. Wickrama (1999), Aircraft emissions: Current inventories and future scenarios, in *Aviation and the Global Atmosphere*, edited by J. Penner et al., chap 9, pp. 291–331, Cambridge University Press, N. York.

Hendricks, J., B. Kärcher, A. Döpelheuer, J. Feichter, U. Lohmann, and D. Baumgardner (2004), Simulating the global atmospheric black carbon cycle: A revisit to the contribution of aircraft emissions, *Atmos. Chem. Phys.*, *4*, 3,521–2,541.

Henne, S., D. Brunner, D. Folini, S. Solberg, J. Klausen, and D. Buchmann (2010), Assessment of parameters describing representativeness of air quality in-situ measurement sites, *Atmos. Chem. Phys.*, *10*, 3,561–3,581.

Herman, R., et al. (2011), Earth Observing System (EOS) Tropospheric Emission Spectrometer (TES) Data Validation Report (Version F06_08), Version 5.0, JPL Internal Report D-33192, April 8, 2012 (available at http://eosweb.larc.nasa.gov/PRODOCS/tes/UsersGuide/TES_L2_Data_Users_Guide.pdf).

Hess, P. G., S. Flocke, J.-F. Lamarque, M. C. Barth, and S. Madronich (2000), Episodic, modeling of the chemical structure of the troposphere as revealed during the spring MLOPEX 2 intensive, *J. Geophys. Res.*, *105*, 26,809–26,839, doi:10.1029/2000JD900253.

Ho, S., D. P. Edwards, J. C. Gille, M. Luo, G. B. Osterman, S. S. Kulawik, and H. Worden (2009), A global comparison of carbon monoxide profiles and column amounts from Tropospheric Emission Spectrometer (TES) and Measurements of Pollution in the Troposphere (MOPITT), *J. Geophys. Res.*, *114*, D21307, doi:10.1029/2009JD012242.

Holloway, T., H. Levy II, and P. Kasibhatla (2000), Global distribution of carbon monoxide, *J. Geophys. Res.*, *105*, 12,123–12,147.

Horowitz, L. W. (2006), Past, present, and future concentrations of tropospheric ozone and aerosols: Methodology, ozone evaluation and sensitivity to aerosol wet removal, *J. Geophys. Res.*, *111*, D22211, doi:10.1029/2005JD006937.

Horowitz, L. W., et al. (2003), A global simulation of tropospheric ozone and related tracers: Description and evaluation of MOZART, version 2, *J. Geophys. Res.*, *108*(D24), 4784, doi:10.1029/2002JD002853.

Horowitz, L. W., A. M. Fiore, G. P. Milly, R. C. Cohen, A. Perring, P. J. Wooldridge, P. G. Hess, L. K. Emmons, and J.-F. Lamarque (2007), Observational constraints on the chemistry of isoprene nitrates over the eastern Unites States, *J. Geophys. Res.*, *112*, D12S08, doi:10.1029/2006JD007747.

Isaksen, I. S. A., et al. (2009), Atmospheric composition change: Chemistry-climate interactions, *Atmos. Environ.*, *43*, 5,138–5,192, doi:10.1016/j.atmos.env.2009.08.003.

Ito, A., S. Sillman, and J. E. Penner (2009), Global chemical transport model study of ozone response to changes in chemical kinetics and biogenic volatile organic compounds emissions due to increasing temperatures: Sensitivities to isoprene nitrate chemistry and grid resolution, *J. Geophys. Res.*, *114*, D09301, doi:10.1029/2008JD011254.

Jaffe, D., A. Mahura, J. Kelley, J. Atkins, P. C. Novelli, and J. Merill (1997), Impact of Asian emissions on the remote North Pacific atmosphere: Interpretation of CO data from Shemya, Guam, Midway, and Mauna Loa, *J. Geophys. Res.*, *102*, 28,627–28,635.

Jöckel, P., et al. (2006), The atmospheric chemistry general circulation model ECAM5/MESSy1: Consistent simulation of ozone from the surface to the mesosphere, *Atmos. Chem. Phys.*, *6*, 5,067–5,104.

John, J., A. M. Fiore, V. Naik, L. W. Horowitz, and J. P. Dunne (2012), Climate versus emission drivers of methane lifetime from 1860–2100, *Atmos. Chem. Phys.*, *12*, 12,021–12,036, doi:10.5194/acp-12-12021-2012.

Kanakidou, M., et al. (2005), Organic aerosol and global climate modeling: A review, *Atmos. Chem. Phys.*, *5*, 1,053–1,123, 1680-7324/acp/2005-5-1053.

Koch, D., and A. D. Del Genio (2010), Black carbon semi-direct effects on cloud cover: Review and synthesis, *Atmos. Chem. Phys.*, *10*, 7,685–7,696, doi:10.5194/acp-10-7685-2010.

Koch, D., S. Menon, A. Del Genio, R. Ruedy, I. Aleinov, and G. A. Schmidt (2009), Distinguishing aerosol impacts on climate over the past century, *J. Climate*, *22*, 2,659–2,677.

Koch, D., et al. (2011), Coupled aerosol-chemistry–climate twentieth-century transient model investigation: Trends in short-lived species and climate responses, *J. Climate*, *24*, 2,693–2,714.

Krol, M., and J. Lelieveld (2003), Can the variability in tropospheric OH be deduced from measurements of 1,1,1-trichloroethane (methyl chloroform)?, *J. Geophys. Res.*, *108*(D3), 4125, doi:10.1029/2002JD002423.

Krol, M., P. J. van Leeuwen, and J. Lelieveld (1998), Global OH trend inferred from methyl chloroform measurements, *J. Geophys. Res.*, *103*, 10,697–10,711.

Kulawik, S. S., J. Worden, A. Eldering, K. Bowman, M. Gunson, G. B. Osterman, L. Zhang, S. Clough, M. W. Shephard, and R. Beer (2006), Implementation of cloud retrievals for Tropospheric Emission Spectrometer (TES) atmospheric retrievals: Part 1. Description and characterization of errors on trace gas retrievals, *J. Geophys. Res.*, *111*, D24204, doi:10.1029/2005JD006733.

Lamarque, J.-F., J. T. Kiehl, P. G. Hess, W. D. Collins, L. K. Emmons, P. Ginoux, C. Luo, and X. X. Tie (2005a), Response of a coupled chemistry-climate model to changes in aerosol emissions: Global impact on the hydrological cycle and the tropospheric burden of OH, ozone, and NO_x, *Geophys. Res. Lett.*, *32*, L16809, doi:10.1029/2005GL023419.

Lamarque, J.-F., P. Hess, L. Emmons, L. Buja, W. Washington, and C. Granier (2005b), Tropospheric ozone evolution between 1890 and 1990, *J. Geophys. Res.*, *110*, D08304, doi:10.1029/2004JD005537.

Lamarque, J.-F., et al. (2010), Historical (1850–2000) gridded anthropogenic and biomass burning emissions of reactive gases and aerosols: Methodology and application, *Atmos. Chem. Phys.*, *10*, 7,017–7,039, doi:10.5194/acp-10-7017-2010.

Lamarque, J.-F., G. P. Kyle, M. Meinshausen, K. Riahi, S. H. Smith, D. P. van Vuuren, A. J. Conley, and F. Vitt (2011), Global and regional evolution of short-lived radiatively-active gases and aerosols in the Representative Concentration Pathways, *Clim. Change*, *109*, 191–212, doi:10.1007/s10584-011-0155-0.

Lamarque, J.-F., et al. (2012), CAM-chem: Description and evaluation of interactive atmospheric chemistry in the Community Earth System Model, *Geosci. Model. Dev.*, *5*, 369–411, doi:10.5194/gmd-5-369-2012.

Lamarque, J.-F., et al. (2013), The Atmospheric Chemistry and Climate Model Intercomparison Project (ACCMIP): Overview and description of models, simulations and climate diagnostics, *Geosci. Model Dev.*, *6*, 179–206, doi:10.5194/gmd-6-179-2013,179-206.

Lawrence, M. G., P. Jöckel, and R. von Kuhlmann (2001), What does the global mean OH concentration tell us?, *Atmos. Phys. Chem.*, *1*, 37–49.

Lee, D. S., B. Owen, A. Graham, C. Fichter, L. L. Lin, and D. Dimitriu (2005), Allocation of International Aviation emissions from scheduled air traffic – Present day and historical (Report 2 of 3), Manchester Metropolitan University, Center for Air Transport and the Environment, CATE-2005-3(C)-2, Manchester, UK. (http://www.cate.mmu.ac.uk/documents/projects/mmuallocationsreport2currentdayv1_5.pdf).

Lee, Y. H., et al. (2013), Evaluation of preindustrial to present-day black carbon and its albedo forcing from ACCMIP (Atmospheric Chemistry and Climate Model Intercomparison Project), *Atmos. Chem. Phys.*, *13*, 2,607–2,634, doi:10.5194/acp-13-2607-2013.

Lelieveld, J., W. Peters, F. J. Dentener, and M. C. Krol (2002), Stability of tropospheric hydroxyl chemistry, *J. Geophys. Res.*, *107*(D23), 4715, doi:10.1029/2002JD002272.

Levy, H., II (1971), Normal atmosphere: Large radical and formaldehyde concentrations predicted, *Science*, *173*, 141–143.

Levy II, H., M. Daniel Schwarzkopf, L. W. Horowitz, V. Ramaswamy, and K. L. Findell (2008), Strong sensitivity of late 21st century climate to projected changes in short-lived air pollutants, *J. Geophys. Res.*, *113*, D06102, doi:10.1029/2007JD009176.

Levy II, H., L. W. Horowitz, M. D. Schwarzkopf, Y. Ming, J.-C. Golaz, V. Naik, and V. Ramaswamy (2013), The roles of aerosol direct and indirect effects in past and future climate change, *J. Geophys. Res. Atmos.*, *118*, 4521–4523, doi:10.1002/jgrd.50192.

Li, F., P. Ginoux, and V. Ramaswamy (2008), Distribution, transport, and deposition of mineral dust in the Southern Ocean and Antarctica: Contribution of major sources, *J. Geophys. Res.*, *113*, D10207, doi:10.1029/2007JD009190.

Liao, H., and J. H. Seinfeld (2005), Global impacts of gas-phase chemistry-aerosol interactions on direct radiative forcing by anthropogenic aerosols and ozone, *J. Geophys. Res.*, *110*, D18208, doi:10.1029/2005JD005907.

Liao, H., P. J. Adams, S. H. Chung, J. H. Seinfeld, L. J. Mickley, and D. J. Jacob (2003), Interactions between tropospheric chemistry and aerosols in a unified general circulation model, *J. Geophys. Res.*, *108*(D1), 4001, doi:10.1029/2001JD001260.

Liao, H., Y. Zhang, W.-T. Chen, F. Raes, and J. H. Seinfeld (2009), Effect of chemistry-aerosol-coupling on predictions of future climate and future levels of tropospheric ozone and aerosols, *J. Geophys. Res.*, *114*, D10306, doi:10.1029/2008JD010984.

Lin, M., et al. (2012a), Transport of Asian ozone pollution into surface air over the western United States in spring, *J. Geophys. Res.*, *117*, D00V07, doi:10.1029/2011JD016961.

Lin, M., O. R. Cooper, L. W. Horowitz, A. O. Langford, H. Levy II, B. J. Johnson, V. Naik, S. J. Oltmans, and C. J. Senff (2012b), Springtime high surface ozone events over the western United States: Quantifying the role of stratospheric intrusions, *J. Geophys. Res.*, *117*, D00V22, doi:10.1029/2012JD018151.

Liu, H., D. J. Jacob, I. Bey, and R. M. Yantosca (2001), Constraints from ^{210}Pb and ^{7}Be on wet deposition and transport in a global three-dimensional chemical tracer model driven by assimilated meteorological fields, *J. Geophys. Res.*, *106*, 12,109–12,128.

Logan, J. A. (1999), An analysis of ozonesonde data for the troposphere: Recommendations for testing 3-D models, and development of a gridded climatology for tropospheric ozone, *J. Geophys. Res.*, *104*, 16,115–16,149.

Logan, J. A., M. J. Prather, S. C. Wofsy, and M. B. McElroy (1981), Tropospheric chemistry: A global perspective, *J. Geophys. Res.*, *86*, 7,210–7,254.

Lohmann, U., and J. Feichter (2005), Global indirect aerosol effects: A review, *Atmos. Chem. Phys.*, *5*, 715–737.

Lohmann, U., L. Rotstayn, T. Storelvmo, A. Jones, S. Menon, J. Quaas, A. M. L. Ekman, D. Koch, and R. Ruedy (2010), Total aerosol effect: Radiative forcing or radiative flux perturbation?, *Atmos. Chem. Phys.*, *10*, 3,235–3,246.

Lopez, J. P., M. Luo, L. E. Christensen, M. Loewenstein, H. Jost, C. R. Webster, and G. Osterman (2008), TES carbon monoxide validation during two AVE campaigns using the Argus and ALIAS instruments on NASA's WB-57F, *J. Geophys. Res.*, *113*, D16S47, doi:10.1029/2007JD008811.

Luo, M., et al. (2007a), Comparison of carbon monoxide measurements by TES and MOPITT: Influence of in situ data and instrument characteristics on nadir atmospheric species retrievals, *J. Geophys. Res.*, *112*, D09303, doi:10.1029/2006JD007663.

Luo, M., et al. (2007b), TES carbon monoxide validation with DACOM aircraft measurements during INTEX-B 2006, *J. Geophys. Res.*, *112*, D24S48, doi:10.1029/2007JD008803.

Madronich, S., and S. Flocke (1998), *The Role of Solar Radiation in Atmospheric Chemistry*, Handbook of Environmental Chemistry, edited by P. Boule, pp. 1–26, Springer-Verland, Heidelberg.

Mahowald, N., D. S. Ward, S. Kloster, M. G. Flanner, C. L. Heald, N. G. Heavens, P. G. Hess, J.-F. Lamarque, and P. Y. Chuang (2011), Aerosol impacts on climate and biogeochemistry, *Ann. Rev. Environ. Res.*, *36*, doi:10.1146/annurev-environ-042009-094507.

Mao, J., et al. (2009), Airborne measurement of OH reactivity during INTEX-B, *Atmos. Chem. Phys.*, *9*, 163–173, doi:10.5194/acp-9-163-2009.

Mao, J., L. W. Horowitz, V. Naik, S. Fan, J. Liu, and A. M. Fiore (2013a), Sensitivity of tropospheric oxidants to wildfires: Implications for radiative forcing, doi:10.1002/grl.50210.

Mao, J., S. Fan, D. J. Jacob, and K. R. Travis (2013b), Radical loss in the atmosphere from Cu-Fe redox coupling in aerosols, *Atmos. Chem. Phys.*, *13*, 509–519, doi:10.5194/acp-13-509-2013.

Martin, R. V., D. J. Jacob, R. M. Yantosca, M. Chin, and P. Ginoux (2003), Global and regional decreases in tropospheric oxidants from photochemical effects of aerosols, *J. Geophys. Res.*, *108*(D3), 4097, doi:10.1029/2002JD002622.

Meinshausen, M., et al. (2011), The RCP greenhouse gas concentrations and their extension from 1765 to 2300, *Clim. Change (Special Issue)*, doi:10.1007/s10584-011-0156-z.

Menon, S., N. Unger, D. Koch, J. Francis, T. Garrett, I. Sednev, D. Shindell, and D. Streets (2008), Aerosol climate effects and air quality impacts from 1980 to 2030, *Environ. Res. Lett.*, *3*, 024,004, doi:10.1088/1748-9326/3/2/024004.

Ming, Y., and V. Ramaswamy (2009), Nonlinear climate and hydrological responses to aerosol effects, *J. Climate*, *22*(6), 1,329–1,339.

Monahan, E. C., D. E. Spiel, and K. L. Davidson (1986), A model of marine aerosol generation via whitecaps and wave disruption, in *Oceanic Whitecaps*, edited by E. C. Monahan, and G. MacNiocaill, pp. 167–174, Reidel, Dordrecht, The Netherlands.

Montzka, S. A., C. M. Spivakovsky, J. H. Butler, J. W. Elkins, L. T. Lock, and D. J. Mondeel (2000), New observational constraints, for atmospheric hydroxyl on global and hemispheric scales, *Science*, *288*, 500–503.

Montzka, S. A., M. Krol, E. Dlugokencky, B. Hall, P. Jöckel, and J. Lelieveld (2011), Small interannual variability of global atmospheric hydroxyl, *Science*, *331*, 67–69.

Naik, V., D. Mauzerall, L. Horowitz, D. Schwarzkopf, V. Ramaswamy, and M. Oppenheimer (2005), Net radiative forcing due to changes in regional emissions of tropospheric ozone precursors, *J. Geophys. Res.*, *110*, D24306, doi:10.1029/2005JD005908.

Naik, V., et al. (2013), Preindustrial to present day changes in tropospheric hydroxyl radical and methane lifetime from the Atmospheric Chemistry and Climate Model Intercomparison Project (ACCMIP), *Atmos. Chem. Phys.*, *13*, 5,277–5,298, doi:10.5194/acp-13-5277-2013.

Naja, M., and S. Lal (2002), Surface ozone and precursor gases at Gadanki (13.5°N, 79.2°E), a tropical rural site in India, *J. Geophys. Res.*, *107*(D14), 4197, doi:10.1029/2001JD000357.

Naja, M., S. Lal, and D. Chand (2003), Diurnal and seasonal variabilities in surface ozone at a high altitude site M. Abu (24.6°N, 72.7°E, 1680 m asl) in India, *Atmos. Environ.*, *37*, 4,205–4,215.

Nassar, R., et al. (2008), Validation of Tropospheric Emission Spectrometer (TES) nadir ozone profiles using ozonesonde measurements, *J. Geophys. Res.*, *113*, D15S17, doi:10.1029/2007JD008819.

Novelli, P. C., and K. A. Masarie (2010), Atmospheric carbon monoxide dry air mole fractions from the NOAA ESRL carbon cycle cooperative global air sampling network, 1988–2009, Version: 2010-07-14, path: ftp://ftp.cmdl.noaa.gov/ccg/co/flask/event/ (downloaded on August 10, 2010).

Novelli, P. C., K. A. Masarie, and P. M. Lang (1998), Distributions and recent changes of carbon monoxide in the lower troposphere, *J. Geophys. Res.*, *103*, 19,015–19,033.

O'Dowd, C. D., M. C. Facchini, F. Cavalli, D. Ceburnis, M. Mircea, S. Decesari, S. Fuzzi, Y. J. Yoon, and J. P. Putaud (2004), Biogenically-driven organic contribution to marine aerosol, *Nature*, *431*, 676–780.

Parrella, J. P., et al. (2012), Tropospheric bromine chemistry: Implications for present and pre-industrial ozone and mercury, *Atmos. Chem. Phys.*, *12*(15), 6,723–6,740.

Philipona, R., K. Behrens, and C. Ruckstuhl (2009), How declining aerosols and rising greenhouse gases forced rapid warming in Europe since the 1980s, *Geophys. Res. Lett.*, *36*, L02806, doi:10.1029/2008GL036350.

Prather, M. J., et al. (2001), Atmospheric chemistry and greenhouse gases, in *Climate Change 2001: The Scientific Basis. Contribution of Working Group I to the Third Assessment Report of the Intergovernmental Panel on Climate Change*, edited by J. T. Houghton et al., pp. 239–287, Cambridge Univ. Press, New York.

Prather, M., C. Holmes, and J. Hsu (2012), Reactive greenhouse gas scenarios: Systematic exploration of uncertainties and the role of atmospheric chemistry, *Geophys. Res. Lett.*, *39*, L09803, doi:10.1029/2012GL051440.

Price, C., and D. Rind (1994), Possible implications of global climate change on global lightning distributions and frequencies, *J. Geophys. Res.*, *99*, 10,823–10,831, doi:10.1029/94JD00019.

Prinn, R. G., R. F. Weiss, B. R. Miller, J. Huang, F. N. Alyea, D. M. Cunnold, P. J. Fraser, D. E. Hartley, and P. G. Simmonds (1995), Atmospheric trends and lifetime of CH_3CCl_3 and global OH concentrations, *Science*, *269*, 187.

Prinn, R., et al. (2001), Evidence for substantial variations of atmospheric hydroxyl radicals in the past two decades, *Science*, *292*, 1,882.

Ramaswamy, V., O. Boucher, J. Haigh, D. Hauglustaine, J. Haywood, G. Myhre, T. Nakajima, G. Y. Shi, and S. Solomon (2001), Radiative forcing of climate change, in *Climate Change 2001: The Scientific Basis: Contribution of WGI to the Third Assessment Report of the IPCC*, edited by J. T. Houghton et al., pp. 349–416, Cambridge Univ. Press, New York.

Rasmussen, D. J., A. M. Fiore, V. Naik, L. W. Horowitz, S. J. McGinnis, and M. G. Schultz (2012), Surface ozone-temperature relationships in the eastern US: A monthly climatology for evaluating chemistry-climate models, *Atmos. Environ.*, *47*, doi:10.1016/j.atmosenv.2011.11.021.

Rayner, N. A., D. E. Parker, E. B. Horton, C. K. Folland, L. V. Alexander, D. P. Rowell, E. C. Kent, and A. Kaplan (2003), Global analyses of sea surface temperature, sea ice, and night marine air temperature since the late nineteenth century, *J. Geophys. Res.*, *108*(D14), 4407, doi:10.1029/2002JD002670.

Reddy, R. R., K. R. Gopal, L. S. S. Reddy, K. Narasimhulu, K. R. Kumar, Y. N. Ahammed, and C. V. K. Reddy (2008), Measurements of surface ozone at semi-arid site Ananatapur (14.62°N, 77.65°E, 331 m asl) in India, *J. Atmos. Chem.*, *59*, 47–59.

Reeve, N., and R. Toumi (1999), Lightning activity as an indication of climate change, *Q. J. R. Meterol. Soc.*, *125*, 893–903.

Reidmiller, D., et al. (2009), The influence of foreign vs. North American emissions on surface ozone in the US, *Atmos. Chem. Phys.*, *9*, 5,027–5,042.

Rosenfeld, D., U. Lohmann, G. B. Raga, C. O'Dowd, M. Kulmala, S. Fuzzi, A. Reissell, and M. O. Andreae (2008), Flood or drought: How do aerosols affect precipitation?, *Science*, *321*, 1,309–1,313.

Ruckstuhl, C., et al. (2008), Aerosol and cloud effects on solar brightening and the recent rapid warming, *Geophys. Res. Lett.*, *35*, L12708, doi:10.1029/2008GL034228.

Sander, S. P., et al. (2006), *Chemical Kinetics and Photochemical Data for Use in Atmospheric Studies*, Evaluation No. 15, JPL Publications 06–2, Jet Propulsion Laboratory, Pasadena, CA, USA.

Schumann, U., and H. Huntrieser (2007), The global lightning-induced nitrogen oxides source, *Atmos. Chem. Phys.*, *7*, 3,823–3,907, doi:10.5194/acp-7-3823-2007.

Shindell, D. T., G. Faluvegi, N. Unger, E. Aguilar, G. A. Schmidt, D. M. Koch, S. E. Bauer, and R. L. Miller (2006a), Simulations of preindustrial, present-day, and 2100 conditions in the NASA GISS composition and climate model G-PUCCINI, *Atmos. Chem. Phys.*, *6*, 4,427–4,459.

Shindell, D. T., et al. (2006b), Multimodel simulations of carbon monoxide: Comparison with observations and projected near-future changes, *J. Geophys. Res.*, *111*, D19306, doi:10.1029/2006JD007100.

Shindell, D. T., G. Faluvegi, S. E. Bauer, D. Koch, N. Unger, S. Menon, R. L. Miller, G. A. Schmidt, and D. G. Streets (2007), Climate response to projected changes in short-lived species under the A1B scenario from 2000–2050 in the GISS climate model. *J. Geophys. Res.*, *112*, D20103, doi:10.1029/2007JD008753.

Shindell, D. T., H. Levy, II, M. D. Schwarzkopf, L. W. Horowitz, J.-F. Lamarque, and G. Faluvegi (2008), Multimodel projections of climate change from short-lived emissions due to human activities, *J. Geophys. Res.*, *113*, D11109, doi:10.1029/2007JD009152.

Shindell, D. T., et al. (2013), Radiative forcing in the ACCMIP historical and future climate simulations, *Atmos. Chem. Phys.*, *13*, 2,939–2,974, doi:10.5194/acp-13-2939-2013.

Skeie, R. B., T. K. Berntsen, G. Myhre, K. Tanaka, M. M. Kvalevåg, and C. R. Hoyle (2011), Anthropogenic radiative forcing time series from pre-industrial times until 2010, *Atmos. Chem. Phys.*, *11*, doi:10.5194/acp-11-11827-2011.

Spivakovsky, C. M., et al. (2000), Three-dimensional climatological distribution of tropospheric OH: Update and evaluation, *J. Geophys. Res.*, *105*, 8,931–8,980.

Stenchikov, G., K. Hamilton, R. J. Stouffer, A. Robock, V. Ramaswamy, B. Santer, and H.-F. Graf (2006), Arctic Oscillation response to volcanic eruptions in the IPCC AR4 climate models, *J. Geophys. Res.*, *111*, D07107, doi:10.1029/2005JD006286.

Stevenson, D. S., et al. (2006), Multi-model ensemble simulations of present day and near-future tropospheric ozone, *J. Geophys. Res.*, *111*, D08301, doi:10.1029/2005JD006338.

Stier, P., J. Feichter, E. Roeckner, S. Kloster, and M. Esch (2006), The evolution of the global aerosol system in a transient climate simulation from 1860 to 2100, *Atmos. Chem. Phys.*, *6*, 3,059–3,076, doi:10.5194/acp-6-3059-2006.

Tie, X. X., S. Madronich, S. Walters, D. P. Edwards, P. Ginoux, N. Mahowald, R. Y. Zhang, C. Lou, and G. Brasseur (2005), Assessment of the global impact of aerosols on tropospheric oxidants, *J. Geophys. Res.*, *110*, D03204, doi:10.1029/2004JD005359.

Tilmes, S., et al. (2012), Ozonesonde climatology between 1995 and 2009: Description, evaluation, and applications, *Atmos. Chem. Phys.*, *12*, 7,475–7,497, doi:10.5194/acp-12-7475-2012.

Tong, D. Q., and D. L. Mauzerall (2006), Spatial variability of summertime tropospheric ozone over the continental United States: Implications of an evaluation of the CMAQ model, *Atmos. Environ.*, *40*, 3,041–3,056, doi:10.1016/j.atmosenv.2005.11.058.

Tost, H., P. Jöckel, and J. Lelieveld (2007), Lightning and convection parameterizations – Uncertainties in global modelling, *Atmos. Chem. Phys.*, *7*, 4,553–4,568, doi:10.5194/acp-7-4553-2007.

Tsigaridis, K., M. Krol, F. J. Dentener, Y. Balkanski, J. Lathière, S. Metzger, D. A. Hauglustaine, and M. Kanakidou (2006), Change in global aerosol composition since preindustrial times, *Atmos. Chem. Phys.*, *6*, 5,143–5,162, doi:10.5194/acp-6-5143-2006.

Turner, A. J., A. M. Fiore, L. W. Horowitz, and M. Bauer (2013), Summertime cyclones over the Great Lakes Storm Track from 1860–2100: Variability, trends, and association with ozone pollution, *Atmos. Chem. Phys.*, *13*, 565–578, doi:10.5194/acp-13-565-2013.

Unger, N., D. T. Shindell, D. M. Koch, and D. G. Streets (2006), Cross influences of ozone and sulfate precursor emissions changes on air quality and climate, *Proc. Natl. Acad. Sci.*, *103*, 4,377–4,380, doi:10.1073/pnas.0508769103.

Unger, N., S. Menon, D. M. Koch, and D. T. Shindell (2009), Impacts of aerosol-cloud interactions on past and future changes in tropospheric composition, *Atmos. Chem. Phys.*, *9*, 4,155–4,129, doi:10.5194/acp-9-4115-2009.

Voulgarakis, A., et al. (2013), Analysis of present day and future OH and methane lifetime in the ACCMIP simulations, *Atmos. Chem. Phys.*, *13*, 2,563–2,587, doi:10.5194/acp-13-2563-2013.

Waliser, D. E., and C. Gautier (1993), A satellite derived climatology of the ITCZ, *J. Clim.*, *6*, 2,162–2,174.

Wang, Y., J. A. Logan, and D. J. Jacob (1998), Global simulation of tropospheric O_3-NO_x-hydrocarbon chemistry, 2. Model evaluation and global ozone budget, *J. Geophys. Res.*, *103*, 10,727–10,756.

Wayne, R. P. (1991), *Chemistry of Atmospheres: An Introduction to the Chemistry of Atmospheres of Earth, the Planets and Their Satellites*, Oxford University Press, New York, 2nd edition, pp.

Wesely, M. L. (1989), Parameterization of surface resistance to gaseous dry deposition in regional-scale numerical models, *Atmos. Environ.*, *23*, 1,293–1,304.

West, J. J., A. M. Fiore, V. Naik, L. W. Horowitz, M. D. Schwarzkopf, and D. L. Mauzerall (2007), Ozone air quality and radiative forcing consequences of changes in ozone precursor emissions, *Geophys. Res. Lett.*, *34*, L06806, 10.1029/2006GL029173.

Wild, O. (2007), Modeling the global tropospheric ozone budget: Exploring the variability in current models, *Atmos. Chem. Phys.*, *7*, 2,643–2,660, doi:10.5194/acp-7-2643-2007.

Wild, O., M. J. Prather, and H. Akimoto (2001), Indirect long-term global radiative cooling from NO_x emissions, *Geophys. Res. Lett.*, *28*, 1,719–1,722.

Williams, E. R. (2009), The global electrical circuit: A review, *Atmos. Res.*, *91*, 140–152, doi:10.1016/j.atmosres.2008.05.018.

Wu, S., L. J. Mickley, D. J. Jacob, J. A. Logan, R. M. Yantosca, and D. Rind (2007), Why are there large differences between models in global budgets of tropospheric ozone?, *J. Geophys. Res.*, *112*, D05302, doi:10.1029/2006JD007801.

Wu, Z., et al. (2012), Evaluation and improvements of two community models in simulating dry deposition velocities for peroxyacetyl nitrate (PAN) over a coniferous forest, *J. Geophys. Res.*, *117*, D04310, doi:10.1029/2011JD016751.

Yienger, J. J., and H. Levy II (1995), Empirical model of global soil-biogenic NO_x emissions, *J. Geophys. Res.*, *100*, 11,447–11,464, doi:10.1029/95JD00370.

Young, P. J., et al. (2013), Pre-industrial to end 21st century projections of tropospheric ozone from the Atmospheric Chemistry and Climate Model Intercomparison Project (ACCMIP), *Atmos. Chem. Phys.*, *13*, 2,063–2,090, doi:10.5194/acp-13-2063-2013.